

Contents lists available at ScienceDirect

Petroleum Science

journal homepage: www.keaipublishing.com/en/journals/petroleum-science



Original Paper

The characteristics and controlling factors of high-quality reservoirs of ultra-deep tight sandstone: A case study of the Dabei Gas Field, Tarim Basin, China



Xiao-Tong Xu ^{a, b, d}, Lian-Bo Zeng ^{a, b, *}, Shao-Qun Dong ^c, Hai-Ming Li ^e, Jian-Zhong Liu ^e, Chun-Qiu Ji ^e

- ^a State Key Laboratory of Petroleum Resources and Engineering, China University of Petroleum (Beijing), Beijing, 102249, China
- ^b College of Geosciences, China University of Petroleum (Beijing), Beijing, 102249, China
- ^c College of Science, China University of Petroleum (Beijing), Beijing, 102249, China
- ^d Hangzhou Research Institute of Geology, PetroChina, Hangzhou, 310023, Zhejiang, China
- ^e Tarim Oilfield Company, PetroChina, Korla, 841000, Xinjiang, China

ARTICLE INFO

Article history: Received 8 July 2024 Received in revised form 29 October 2024 Accepted 24 March 2025 Available online 24 March 2025

Edited by Xi Zhang and Jie Hao

Keywords:
Ultra-deep
Tight sandstone gas reservoir
Diagenetic facies
High-quality reservoir
Characteristic and controlling factors
Evolution and distribution

ABSTRACT

High-quality reservoirs with sufficient physical properties of ultra-deep tight gas reservoirs in the Lower Cretaceous Bashijiqike Formation exhibit significant relationship with gas production across the Dabei Gas Field. Clarifying the characteristics, controlling factors, evolution and distribution of the high-quality reservoirs is important for the deployment of "sweet spots". An integrated approach of petrography, SEM, cathode luminescence, XRD, physical property, NMR experiment, well logs and 3D pre-stack depth migration data was carried out. This study examined the sedimentation, diagenesis, tectonism, gypsumrock and overpressure to reveal the formation and distribution of the high-quality reservoirs. The sandstones are very fine-to coarse-grained lithic arkose. The variation in detrital grains texture and mineralogical composition affects diagenetic evolution, pore structure and gas-bearing characteristic. Three diagenetic facies (diagenetic facies A to C) are classified. Different diagenetic facies underwent different evolution of reservoir quality. The medium-fine to medium-grained lithic arkose (diagenetic facies A) underwent medium vertical compaction, tectonic compression and cementation, and exhibited relatively porous, which makes partial primary pores preserved with the occurrence and persistence of overpressure. Conversely, the very fine to fine-grained and mud gravel-rich medium-grained lithic arkose (diagenetic facies B) and diagenetic facies C appeared premature densification by strong compaction and tight carbonate cementation, respectively, which makes them free from overpressure effects. Natural fractures increased the permeability by several orders of magnitude. Gypsum-rock weakened the vertical compaction and tectonic compression, and delayed cementation, promoted and preserved overpressure. With the injection of internal high alkaline fluids, anhydrite/dolomite cements/ veins and dissolution of siliceous developed. Diagenetic facies A exhibited sufficient physical properties and gas volume, making it the high-quality reservoir in tight gas sandstone. Diagenetic facies B and C mainly were used as barriers for hydrocarbon charging. Diagenetic facies A was mainly distributed in the middle-lower part of distributary channel or the middle-upper part of mouth bar. This distribution model provides guidance for exploration in ultra-deep tight sandstone gas reservoir.

© 2025 The Authors. Publishing services by Elsevier B.V. on behalf of KeAi Communications Co. Ltd. This is an open access article under the CC BY-NC-ND license (http://creativecommons.org/licenses/by-nc-nd/

4.0/).

1. Introduction

Hydrocarbon exploration has fully entered the historical stage of "deep, deep water and unconventional" in China (Jia, 2023). Based on Chinese exploration practice, domains with burial depth exceeding 4500 m in western basin and exceeding 6000 m in

E-mail address: lbzeng@sina.com (L.-B. Zeng).

Peer review under the responsibility of China University of Petroleum (Beijing).

^{*} Corresponding author.

eastern basin are collectively referred to as ultra-deep (Cao et al., 2022). Under comprehensive effects of sedimentation, diagenesis and tectonism, the spatial distribution and various internal properties of the ultra-deep tight sandstone reservoir have very uneven changes, which exhibits strong heterogeneity (Pettijohn et al., 1972; Weber, 1986; Pranter and Sommer, 2011; Luo et al., 2020). Hydrocarbon usually gather in the domain (high-quality reservoir) of relatively good physical properties (Bloch et al., 2002; Bjørlykke, 2014; Cao et al., 2017; Luo et al., 2023a; Cao et al., 2024a). Accordingly, understanding the characteristic and controlling factors of high-quality reservoir is an important step in the exploration and development of ultra-deep oil and gas.

Reservoir quality of ultra-deep tight sandstone appears structural under the control of sedimentation and tectonism, which shows obvious differences in composition and texture of detrital grains, diagenesis, petrophysical properties, pore structure and fluid flow (Luo et al., 2016, 2023b; Cao et al., 2023). Litho facies, petrofacies and diagenetic facies are always implied to evaluate reservoir quality (Grigsby and Langford, 1996; Rushing et al., 2008; Cao et al., 2020; Yang et al., 2022). Diagenetic facies are results of the comprehensive action of structure, fluid, temperature and pressure on sediments (Zou et al., 2008). It is better to study the formation mechanism, spatial distribution and quantitative evaluation of reservoirs (Lai et al., 2018). Generally, compaction and cementation mainly result in reservoir densification, while dissolution is the key to improve reservoir quality (Dutton and Loucks, 2010; Busch et al., 2019; Yuan et al., 2019). Compared to the middle-shallow, diagenesis exhibits stronger heterogeneity and complexity in deep-ultra-deep tight sandstone (Dutton et al., 2012; Cao et al., 2021). In addition, grain coating, overpressure, hydrocarbon charging and fracture also show significantly effects on reservoir quality (Aase et al., 1996; Lander et al., 2008; Taylor et al., 2010; Worden et al., 2020; Xu et al., 2023; Zeng et al., 2024).

Tectonism also has significant effects on the formation and evolution of ultra-deep tight sandstone reservoir, especially in zones with strong tectonic deformation. Structural diagenesis refers to the interplay of structure and diagenesis interaction in the process of sedimentary rock from loose sediment to consolidation into rock and thereafter (Laubach et al., 2010; Zeng et al., 2016a). It is often used to characterize diagenetic and storage processes of sediments involved in tectonism (Vandeginste et al., 2012; Ferraro et al., 2019). Tectonism controls provenance of sediments and affect accumulation pattern, development location and filling pattern of sediments (Zhang et al., 2021c; Pizzi et al., 2023). Strong tectonic compression leads to porosity loss and the development of overpressure (Guo et al., 2016a; Wei et al., 2022). Tectonic fractures improve reservoir quality and serve as "highway" for fluid migration (Zeng et al., 2010; Zeng et al., 2022; Cao et al., 2024b).

This paper focuses on the Lower Cretaceous Bashijiqike Formation of Dabei Gas Field, Tarim Basin. Characteristics of petrology, diagenesis and natural fracture have been sorted out in previous studies (Li et al., 2017; Guo et al., 2018). Continuous burial compaction, strong tectonic compression and multiple cementations result in reservoir densification (Shou et al., 2009; Gao et al., 2018; Zhang et al., 2021b). Dissolution and natural fractures are keys for highquality reservoirs (Gao et al., 2017; Lai et al., 2022). The previous studies also carried on a certain discussion on the identification of diagenetic facies. Combined with diagenetic intensity and authigenic minerals content, the ultra-deep tight sandstone reservoirs are classified into three diagenetic facies: carbonate cemented facies, tightly compacted facies, slightly cemented and compacted facies, and then are predicted by well logs (Lai et al., 2018, 2023). Based on texture and detrital grains composition, detrital matrix, diagenesis, and pore types, three petrofacies are classified: ductile-lean sandstone, ductile-rich sandstone and tightly calcite-cemented sandstone

(Liu, 2021; Zhang et al., 2021a). The characteristics and controlling factors of high-quality reservoirs remains ambiguous, making it difficult for efficient exploration. This paper aims to clarify the relationships between texture and composition of detrital grains, differential diagenesis, tectonism and the evolution of high-quality reservoirs of ultra-deep tight sandstone, and then establish a conceptual model for evolution and distribution of high-quality reservoirs. This study employed an integrated approach including cores. thin sections, SEM, cathode luminescence, XRD, physical property, NMR experiment, well logs and 3D pre-stack depth migration data. The goals are to (1) investigate the texture and composition of detrital grains, authigenic minerals, pore structure, natural fractures of the Bashijiqike Formation tight gas sandstones, (2) clarify differential reservoir quality, the type and characteristic of high-quality reservoirs, (3) examine the controlling factors of high-quality reservoirs, and (4) establish the evolution and distribution of high-quality reservoirs.

2. Geological setting

2.1. Location and structure

The Kuqa depression is located in the northern margin of Tarim Basin, western China (Fig. 1(a)). Since the late Hercynian period, it has undergone several evolutionary stages, such as late Permian-Triassic paleo-foreland basin, Jurassic-Paleogene extensional depression basin and Neogene-quaternary intracontinental foreland basin (Qin et al., 2022). It eventually develops into a meso-Cenozoic superimposed foreland basin on the basis of Paleozoic passive continental margin (Jia et al., 2023). The Kuqa depression is adjacent to the southern Tianshan orogenic belt in the north and the Tabei Uplift in the south, with a total area of $3.7 \times 10^4 \ \text{km}^2$ (Fig. 1(b)). It is composed of the Northern monoclinal belt, the Kelasu tectonic belt, the Yiqikelike tectonic belt, the Qiulitage tectonic belt, the Southern slope belt, the Baicheng sag, the Yangxia sag and the Wushi sag.

The Kelasu tectonic belt exhibits NEE–SWW distribution (Fig. 1(b)). From west to east, it is successively Awat zone, Bozi zone, Dabei zone and Keshen zone. Controlled by strong thrust napper of the southern Tianshan Mountains, the Dabei zone exhibits an imbricated tectonic belt (Wang et al., 2022). It is composed of several faulted anticlines or fault nose structures, and develops a series of northerly thrust faults and some southerly thrust faults (Fig. 1(c)). The first-order faults are the Baicheng fault and the Kelasu fault. The second-order faults are F1, F2, F3, F4, F5, F6 (Fig. 1(d)). Some third-order faults and a large number of small faults are developed in the gas reservoir.

2.2. Stratigraphy

The drilling reveals Triassic, Jurassic, Cretaceous, Paleogene, Neogene and Quaternary strata (Fig. 1(e)). The Lower Cretaceous Bashijiqike Formation (K_1bs) is the most important gas-bearing formation, with burial depth 5000–8000 m. It is vertically divided into K_1bs^1 , K_1bs^2 and K_1bs^3 . The uplift and erosion of the Late Cretaceous leads to the denudation of the Upper Cretaceous and the K_1bs^1 (Jiang et al., 2015). The K_1bs^2 is in unconformable contact with the overlying Kumugeliemu Group ($E_{1-2}km$) (Fig. 1(e)). The K_1bs^2 is the braided river delta front deposit and the K_1bs^3 is the fan delta front deposit. Sand bodies are large thickness, far extension, and continuous distribution laterally. Vertically, multistage sand bodies are superimposed on each other, with thin and laterally discontinuous mudstones inside. The Triassic–Jurassic lacustrine coal seam are the most important source rocks with large thickness and strong hydrocarbon generation intensity (Shen

X.-T. Xu, L.-B. Zeng, S.-Q. Dong et al. Petroleum Science 22 (2025) 3473—3496

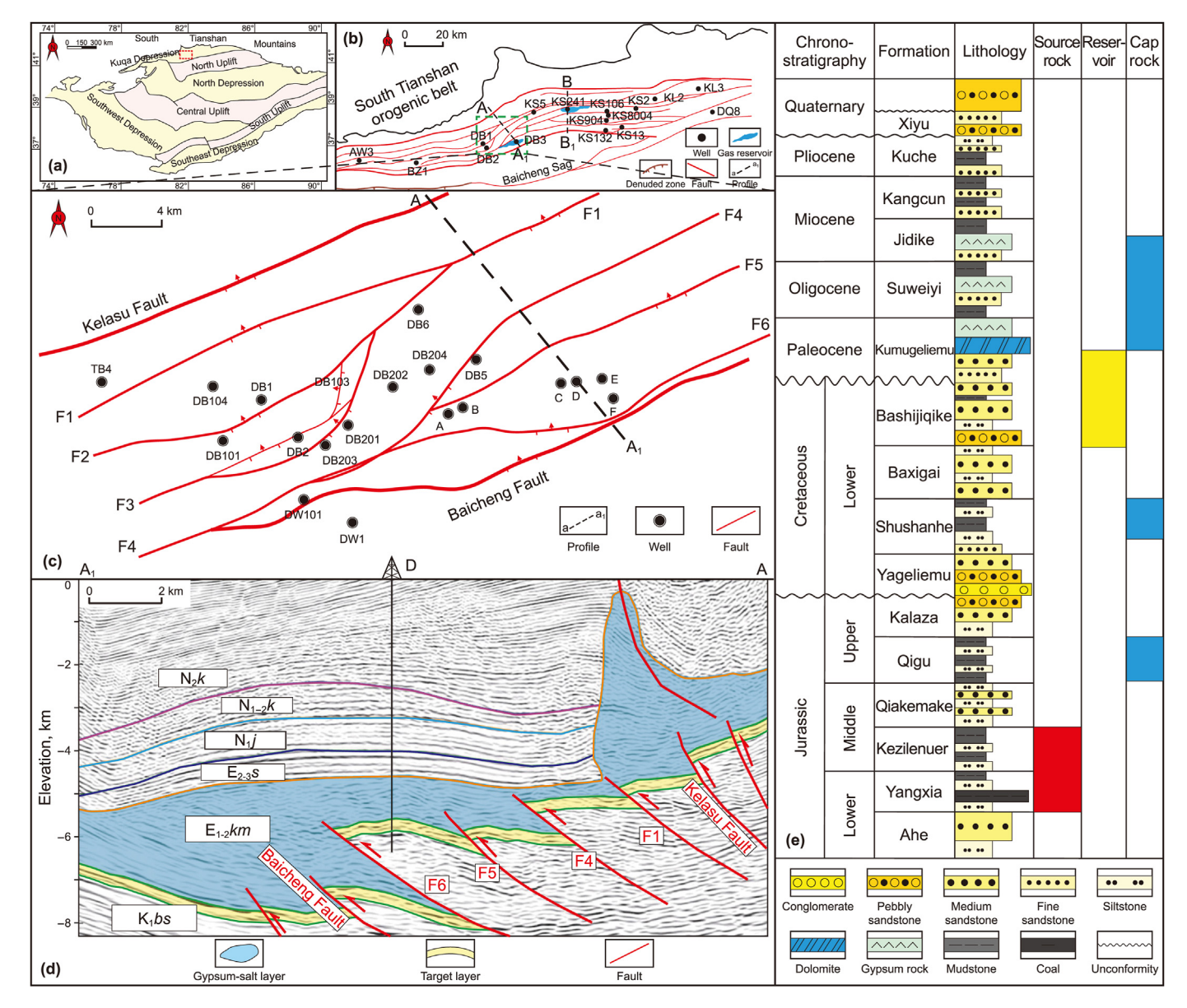


Fig. 1. (a) Location of the Kuqa depression. (b) Distribution of the Dabei 3 gas reservoir in the Kelasu tectonic belt and tectonic cross-section AA₁ and BB₁. (c) Plane structure map of the Dabei 3 gas reservoir. (d) Tectonic cross-section AA₁ (modified after Li et al., 2020). (e) Comprehensive stratigraphy of the Kuqa depression.

et al., 2017; Wang et al., 2023). The overlying huge thick gypsumsalt rock serves as the main regional cap layer. Controlled by strong uplift and compression nappe of the southern Tianshan Mountains, numerous thrust imbricate fault anticlines develop in the subsalt (Fig. 1(d)). Dabei 1, Dabei 2 and Dabei 3 gas reservoirs have been found in the subsalt, showing good exploration and development prospects (Fig. 1(b)).

3. Material and methods

Samples are mainly from Wells B, C, E and F in Dabei 3 gas reservoir (Fig. 1(c)). Cores were described in detail, including lithology, sedimentary structure, natural fractures.

3.1. Petrographic analysis

A total of 35 samples were selected to make thin sections to analyze petrographic characteristics. Alizarin red-S and K-ferricyanide were used for staining to distinguish between different carbonate minerals (calcite was stained red). Using ZEISS Scope. A1 polarizing microscope, the percentages of composition, authentical minerals and pores were determined by Gazzi-Dickinson point counting (William and Christopher, 1979), with each thin section 300 points. Using the Quanta200 scanning electron microscope (SEM) equipped with EDAX spectrometer working at an acceleration voltage of 20 kV and a beam current of 4 nA, the type and micro texture of diagenetic minerals were further identified. The LABORLUX-12POL polarizing microscope equipped with ELM-3RX cathode luminescence instrument was used to identify mineral types and differentiate formation stages.

Based on the results of thin section identification, the compactional porosity loss (COPL) and cementational porosity loss (CEPL) are quantitatively evaluated by the formulas proposed by Lundegard (1992).

$$COPL = P_{i} - \frac{(100 - P_{i}) \cdot P_{mc}}{(100 - P_{mc})}$$
 (1)

$$CEPL = (P_i - COPL) \cdot \frac{C}{P_{mc}}$$
 (2)

$$ICOMPACT = \frac{COPL}{COPL + CEPL}$$
 (3)

where P_i is the primary porosity, %; P_{mc} is the intergranular volume (IGV), %; C is the total cement volume, %; ICOMPACT is the compaction index.

3.2. Grain size analysis

The screening method was performed by the Chinese standard "SY/T 5434–2009". A total of 35 samples were broken and ground in the disintegrator, without destroying grains. Subsequently, samples were completely sieved, and separated by different grain size in the 200-sieve shaker. By weighing the quality of different series, the distribution of grain size was obtained. On this basis, P_i was calculated by the empirical formula proposed by Beard and Weyl (1973) (Table 1).

$$P_{\rm i} = 20.91 + \frac{22.90}{S_{\rm o}} \tag{4}$$

$$S_0 = \sqrt{\frac{Q_1}{Q_3}} \tag{5}$$

where S_0 is the Trask sorting coefficient; Q_1 , Q_3 are the grain size corresponding to the values of 25% and 75% on the probability cumulative curve, mm (Trask, 1930).

3.3. Physical properties measurements

According to Chinese standard "SY/T 5336–2006", a total of 155 samples were tested for helium porosity through the extended range helium pore gauge equipped with the ZYB-IB vacuum pressure saturation device (experimental temperature 26 °C, atmospheric pressure 0.090 MPa). The samples were also tested for permeability through the DX-07G gas permeability tester equipped with the ZYB-IB vacuum pressure saturation device (experimental temperature 29 °C, atmospheric pressure 0.090 MPa). On the basis, three samples with fractures were tested for full diameter core physical properties (experimental temperature 21 °C, atmospheric pressure 0.092 MPa).

3.4. Porosity loss by tectonic compression

Porosity loss by tectonic compression is the difference between the total porosity loss by compaction and the porosity loss by burial compaction (Wei et al., 2022).

$$\Phi_{\mathsf{Co}} = \Phi_{\mathsf{P}} - \Phi_{\mathsf{M}} + \Phi_{\mathsf{D}} - \Phi_{\mathsf{Ce}} \tag{6}$$

$$\Phi_{\mathsf{T}} = \Phi_{\mathsf{CO}} - \Phi_{\mathsf{B}} \tag{7}$$

where Φ_{Co} is the total porosity loss by compaction, %; Φ_P is the primary porosity, %; Φ_M is the core-measured porosity, %; Φ_D is the porosity incremental by dissolution, %; Φ_{Ce} is the porosity loss by cementation, %; Φ_T is the porosity loss by tectonic compression, %; Φ_B is the porosity loss by burial compaction, %.

 $\Phi_{\rm B}$ is derived from the empirical formula summarized by Shou et al. (2006) through the compaction simulation experiment. In the compaction simulation experiment, the standard samples are

medium-fine to medium-grained sandstones with medium sorting, mud content less than 2%, cements content ranging from 2% to 5%, and primary pores dominant.

$$\Phi_{\rm B}$$
=0.01*D* × 1.0578e^{-0.0103}T, ΔT =2.0-3.5 °C/100 m (8)

$$\Phi_{\rm B}$$
=0.01D × 1.6704e^{-0.0075T}, ΔT =3.5-4.5 °C/100 m (9)

where D is the maximum paleo-burial depth, m; T is the paleo-formation temperature corresponding to the maximum paleo-burial depth, °C; ΔT is the paleo-geothermal gradient, °C/100 m.

3.5. NMR experiment

According to Chinese standard "SY/T 6490-2007", a total of 23 samples were tested for pore size and gas saturation through the CoreSpec-1000NMR core analyzer, HR2500-2 high speed freezing centrifuge and AE200 electronic balance (indoor temperature: 20-25 °C, humidity: 50%-70% RH). The experimental steps are mainly as follows: (1) The plunger cores were vacuumized and saturated with water. (2) The T_2 spectrum of each rock sample was measured by NMR scanning. (3) Under the given pressure condition, each rock sample was dehydrated by the centrifuge until each rock sample was in the state of saturated bound water. (4) The T_2 spectrum of each rock sample was measured again by NMR scanning. Based on the model of pore diameter of NMR, pores with different pore diameter exhibit different specific surface, and then are corresponding to different NMR relaxation rates. The transverse relaxation time of macropores is long, while that of small pores is short. Based on $T_2 = mr^n$ (Song et al., 2024), the transverse relaxation (ms) is transformed into pore diameter (µm). Bound water saturation is the ratio of the area of the T_2 spectrum after centrifugation to the area of the T_2 spectrum of saturated water. Therefore, gas saturation can be defined as follow:

Gas saturation =
$$100$$
-bound water saturation (10)

On the basis, the gas volume can be defined as follow:

Gas volume = gas saturation
$$\times$$
 total pore volume (11)

4. Results

4.1. Petrology and mineralogy

The Bashijiqike Formation sandstones exhibit very fine to coarse-grained, mainly fine and medium-grained, with the median grain size values mainly ranging from 88.45 to 230.16 μ m (Table 1). Detrital grains are mainly subangular and subangular to subrounded. Grain sorting is medium to good, with the trask sorting coefficient (S_0) ranging from 1.398 to 2.274 (average 1.751) (Table 1).

Sandstones are lithic arkose (Fig. 2(a)). The contents of detrital quartz grains range from 38% to 49% (average 43.4%). Most of them are monocrystalline, and the rest are polycrystalline of metamorphic origin with wavy extinction. The contents of K-feldspar grains are 18%–25% (average 21.6%), and the contents of plagioclase are 10%–17% (average 12.6%) (Table 1). Volcanic rock fragments are the most abundant lithic components (Fig. 2(b)), with the contents from 7% to 15% (average 11.0%) (Table 1). It can be seen that different igneous textures in thin section, such as trachytic, felsitic, spheroidal, microcrystalline and cryptocrystalline type. The contents of metamorphic rock fragment are 5%–13% (average 8.8%)

Petroleum Science 22 (2025) 3473-3496

Table 1Results of point counting and sample petrophysical properties.

Well	Depth,	Diagenetic facies	ection poros	ity		Textural characteris	ral characteristic					Detrital grains					
	m		Porosity, %	Permeability, 10 ⁻³ μm ²	Total, %	Primary, %	Secondary, %	Fracture, %	Median grain size, μm	Roundness	Q ₁ , mm	Q₃, mm	So	P _i , %	Quartz, %	K-feldspar, %	Plagioclase, %
В	6978.73	С	2.74	0.024	0.00	0.00	0.00	0.00	219.22	SA-SR	0.463	0.090	2.274	30.982	42.00	22.00	13.00
В	7026.77	В	3.64	0.034	1.00	0.33	0.33	0.33	145.57	SA-SR	0.227	0.081	1.676	34.574	42.00	25.00	13.00
В	7027.96	В	5.27	0.039	2.00	0.33	1.67	0.00	167.67	SA-SR	0.248	0.080	1.759	33.927	44.00	25.00	14.00
В	7029.04	В	5.86	0.059	1.67	0.33	1.33	0.00	147.70	SA	0.228	0.046	2.227	31.194	47.00	25.00	15.00
В	7031.08	В	3.40	0.021	1.00	0.00	0.33	0.67	164.03	SA	0.295	0.097	1.847	33.310	42.00	20.00	13.00
В	7030.35	В	1.62	0.025	0.33	0.00	0.33	0.00	148.69	SA	0.222	0.092	1.553	35.656	43.00	23.00	12.00
В	7031.78	В	5.13	0.087	2.00	0.33	1.67	0.00	196.11	SA	0.387	0.079	2.211	31.265	43.00	21.00	15.00
В	7031.91	В	3.64	0.034	1.33	0.33	0.67	0.33	165.82	SA	0.225	0.073	1.753	33.972	42.00	23.00	12.00
В	7032.66	В	4.21	0.039	1.33	0.00	1.33	0.00	161.65	SA	0.227	0.078	1.705	34.339	39.00	23.00	14.00
В	7075.38	C	1.71	0.024	0.00	0.00	0.00	0.00	91.23	SA	0.243	0.063	1.939	32.723	47.00	24.00	14.00
В	7075.67	В	2.17	0.008	0.67	0.00	0.00	0.67	110.60	SA	0.199	0.074	1.636	34.909	38.00	23.00	17.00
В	7076.52	В	2.02	0.018	0.67	0.00	0.33	0.33	114.34	SA	0.247	0.053	2.151	31.556	42.00	20.00	14.00
В	7080.46	В	2.61	0.023	1.00	0.00	0.67	0.33	111.26	SA	0.207	0.072	1.693	34.432	43.00	20.00	12.00
Е	7210.15	В	5.38	0.112	2.67	0.33	2.33	0.00	212.14	SA	0.306	0.079	1.968	32.545	49.00	20.00	12.00
E	7210.89	A	9.83	7.770	6.33	3.00	3.00	0.33	229.93	SA-SR	0.241	0.122	1.409	37.159	44.00	20.00	11.00
Е	7212.79	Α	7.59	0.248	3.33	1.33	2.00	0.00	218.73	SA-SR	0.264	0.135	1.398	37.286	44.00	20.00	12.00
Е	7214.94	Α	8.90	0.326	4.67	2.67	2.00	0.00	168.34	SA-SR	0.212	0.097	1.479	36.389	44.00	21.00	11.00
Е	7215.87	Α	10.14	2.050	7.33	4.67	2.67	0.00	201.84	SA-SR	0.214	0.073	1.712	34.285	45.00	20.00	14.00
E	7217.90	В	6.60	0.244	2.33	1.67	0.67	0.00	182.35	SR	0.346	0.140	1.575	35.453	43.00	20.00	12.00
E	7219.30	A	8.79	0.417	5.33	3.00	2.33	0.00	185.59	SA	0.205	0.087	1.535	35.828	45.00	21.00	10.00
E	7220.16	A	10.86	4.870	7.00	4.67	2.33	0.00	178.36	SA-SR	0.227	0.094	1.554	35.646	46.00	20.00	10.00
E	7221.23	A	9.92	0.945	5.00	3.00	2.00	0.00	182.87	SA	0.225	0.103	1.479	36.389	46.00	20.00	10.00
E	7221.65	A	9.77	0.753	5.67	3.00	2.67	0.00	193.76	SA	0.205	0.081	1.591	35.305	44.00	20.00	11.00
E	7222.58	A	11.55	11.200	8.00	4.67	3.33	0.00	198.60	SA	0.227	0.104	1.479	36.389	43.00	20.00	11.00
E	7223.14		8.89	1.410	7.67	4.67	3.00	0.00	219.88	SA	0.240	0.093	1.608	35.154	44.00	21.00	12.00
E	7223.68	A	9.75	6.120	8.67	4.67	4.00	0.00	230.16	SA-SR	0.316	0.126	1.586	35.353	45.00	20.00	10.00
E	7224.43	A	6.70	0.234	4.00	2.67	1.33	0.00	193.73	SA-SR	0.212	0.091	1.526	35.914	43.00	21.00	12.00
E	7225.17	A	7.06	0.540	3.67	2.33	1.33	0.00	164.26	SA	0.193	0.081	1.542	35.759	41.00	21.00	12.00
E	7290.33	В	3.26	0.030	0.67	0.33	0.33	0.00	158.69	SA	0.225	0.073	1.753	33.972	41.00	25.00	13.00
E	7291.19	В	2.81	0.075	0.67	0.00	0.33	0.33	147.24	SA	0.241	0.074	1.803	33.615	41.00	25.00	16.00
E	7292.47	В	4.61	0.038	0.67	0.00	0.67	0.00	113.65	SA	0.245	0.064	1.959	32.601	42.00	25.00	14.00
E	7296.39	C	1.38	0.012	0.00	0.00	0.00	0.00	95.60	SA	0.227	0.064	1.879	33.097	45.00	20.00	12.00
E	7298.90	В	4.91	0.135	3.00	0.33	2.67	0.00	162.17	SA	0.268	0.081	1.821	33.483	44.00	24.00	16.00
E	7365.53	C	0.90	0.020	0.00	0.00	0.00	0.00	143.06	SA-SR	0.228	0.046	2.227	31.194	42.00	20.00	11.00
E	7367.58		3.07	0.020	0.33	0.00	0.33	0.00	88.45	SA-SR	0.232	0.040	1.972	32.520	44.00	18.00	12.00
			3.07	0.007	0.55	0.00	0.33	0.00			0.232	0.000	1,312	32,320	-1-1.00	10.00	12.00
Well	Depth,	Detrital grains							Authigenic	minerals							
weii	m		ent, Metai	morphic rock fra	gment,	Sedimenta	ry rock fragme	ent, Mica,	Matrix, Calcite, F		lomite,	Ankerite	, Quart	z overgro	wth, Albi	i	ite, Anhydrite

Well	Depth, m	Detrital grains						Authigenic minerals							
		Volcanic rock fragment, %	Metamorphic rock fragment, %	Sedimentary rock fragment, %	Mica, %	Matrix, %	Calcite, %	Fe-calcite, %	Dolomite, %	Ankerite, %	Quartz overgrowth, %	Albite, %	Anhydrite, %	Hematite, %	
В	6978.73	13.00	8.00	2.00	0.00	1.00	18.00	0.00	0.00	0.00	0.00	0.00	0.00	0.33	
В	7026.77	10.00	8.00	2.00	2.33	2.00	2.00	0.00	0.00	0.67	2.00	1.00	0.00	2.00	
В	7027.96	9.00	6.00	2.00	0.00	3.00	3.00	0.00	0.00	0.33	2.33	1.00	0.33	0.00	
В	7029.04	7.00	5.00	1.00	0.00	1.00	1.00	0.00	0.00	0.00	3.00	2.00	0.00	0.00	
В	7031.08	12.00	10.00	3.00	1.33	3.00	4.67	0.00	0.00	0.00	2.00	1.33	0.00	0.00	
В	7030.35	12.00	8.00	2.00	0.00	6.00	1.00	0.00	0.00	0.33	0.33	0.67	0.00	0.67	
В	7031.78	11.00	8.00	2.00	0.00	2.00	4.00	0.00	0.00	0.00	2.00	1.00	0.33	0.33	
В	7031.91	12.00	9.00	2.00	0.00	4.00	1.67	0.00	0.00	0.00	2.33	1.00	0.00	0.00	
В	7032.66	14.00	8.00	2.00	0.33	3.00	2.33	0.00	0.00	0.00	1.67	1.00	0.00	0.67	
В	7075.38	8.00	6.00	1.00	0.33	2.00	25.00	0.00	0.00	0.00	0.00	0.00	0.00	0.00	
В	7075.67	12.00	8.00	2.00	0.67	1.00	1.00	0.33	0.00	0.00	1.00	1.00	0.00	0.33	
В	7076.52	14.00	8.00	2.00	0.00	5.00	3.00	0.00	0.00	0.00	2.00	1.00	0.00	0.00	
В	7080.46	15.00	8.00	2.00	0.00	4.00	3.00	0.00	0.00	0.00	2.00	1.00	0.00	0.00	

(continued on next page)

Table 1 (continued)

),67),000),33),33),33),33),000 75% on the probability cumulative curve, mm. Anhydrite,),000),000),000),007),007),007),000 Albite, Quartz overgrowth, Ankerite, the values of 25% and), 333), 333), 500), Dolomite, Authigenic minerals Fe-calcite, Subangular; SR = Subrounded; M = Medium; G = Good; S_o = The Trask sorting coefficient; Q₁, Q₃ are the grain size corresponding to Calcite, Matrix, Mica, Sedimentary rock fragment, Metamorphic rock fragment, Volcanic rock fragment, Detrital grains 7291.19 7292.47 7296.39 7217.90 7223.14 7220.16 7221.65 7219.30 7223.68 7224.43 7225.17 7290.33 Depth, Ε Well ^kSA

(Table 1). They mainly consist of metamorphic quartzite and various low-grade metamorphic rock fragments, such as schist, slate, phyllite and metamorphic siltstone. Sedimentary rock fragments have contents of 1%–5% (average 2.5%) (Table 1). They are mainly chert and mudstone. Mud gravels are abundant locally. In addition, micas occur in trace amounts, up to 2.33% (Table 1).

4.2. Diagenetic characteristics

4.2.1. Compaction

With increases of overlying load, grains gradually displace and deform, and then become close to each other. Ductile grains (low-grade metamorphic rock fragments, altered volcanic rock fragments, mudstone, mica and mud gravel) are usually bent and deformed along rigid grains (quartz, feldspar and high-grade metamorphic rock fragments) (Fig. 3(a)). Partial strongly deformed ductile grains are squeezed into pores to form pseudomatrix. Partial quartz and feldspar are squeezed into the mud gravel, resulting in local densification (Fig. 3(b)). In addition, as the burial depth increases, mechanical compaction gradually transforms into chemical compaction (Bjørlykke, 2014). It mainly exhibits pressure dissolution between quartz grains. The N–S direction strong tectonic compression in the late Himalayan period also causes horizontal compaction (Zeng et al., 2022).

Influenced by detrital grains texture and mineralogical composition, sandstones exhibit differential compaction. For relatively finer-grained sandstones, strong deformation of ductile grains results in very few primary pores (Fig. 3(a)). The sandstones exhibit strong compaction. For relatively coarser-grained sandstones, grains generally show point—line contact, and primary pores and dissolved pores develop (Fig. 3(c)). The sandstones exhibit medium compaction. For sandstones tightly cemented by carbonate cements, grains exhibit "floating", and ductile grains have less deformation (Fig. 3(d)). The sandstones exhibit weak compaction.

4.2.2. Cementation

Main authigenic minerals are calcite, dolomite, quartz, albite, anhydrite, clay minerals and hematite. The content of calcite ranges from 0% to 27%, the content of dolomite ranges from 0% to 11%, the content of quartz ranges from 0% to 4%, the content of albite ranges from 0% to 2%, the content of anhydrite ranges from 0% to 4%, the content of hematite is less than 1% (Fig. 4(a)).

Both calcite and dolomite exhibit three types. The first type is poikilitic (Fig. 3(d)). Calcite/dolomite tightly cements pores and metasomatizes grain boundary. The second type exhibits mediumcoarse xenomorphic granular (Fig. 3(e)). Calcite cements partial pores and metasomatizes partial grains or quartz/feldspar overgrowths. The third type is fracture vein (Fig. 3(f)). Anhydrite exhibit two types. The first type is medium-coarse xenomorphic granular (Fig. 3(g)). The second type is fracture vein (Fig. 3(h)). Ouartz/ feldspar overgrowth mostly exhibit I-overgrowth. II-overgrowth can be seen locally (Fig. 3(e) and (i)). Hematite is in the form of grain coating (Fig. 3(d)). It can be seen that quartz/feldspar completely covered by hematite coating exhibits overgrowth (Fig. 3(i)), indicating that hematite coating cannot inhibit overgrowth. XRD analysis shows that clay minerals are illite/smectite (average 10.29%), illite (average 50.47%), kaolinite (average 14.59%), chlorite (average 24.64%) (Fig. 4(b)). Illite fills intergranular pores in the form of hairlike (Fig. 3(m)).

4.2.3. Dissolution

Dissolution is widely developed and mainly occurs in relatively coarser-grained sandstones with little matrix. It mainly exhibits the dissolution of grains (quartz, feldspar, rock fragment) (Fig. 3(b), (n) and (o)) and cements (calcite, feldspar overgrowth) (Fig. 3(i), (k)

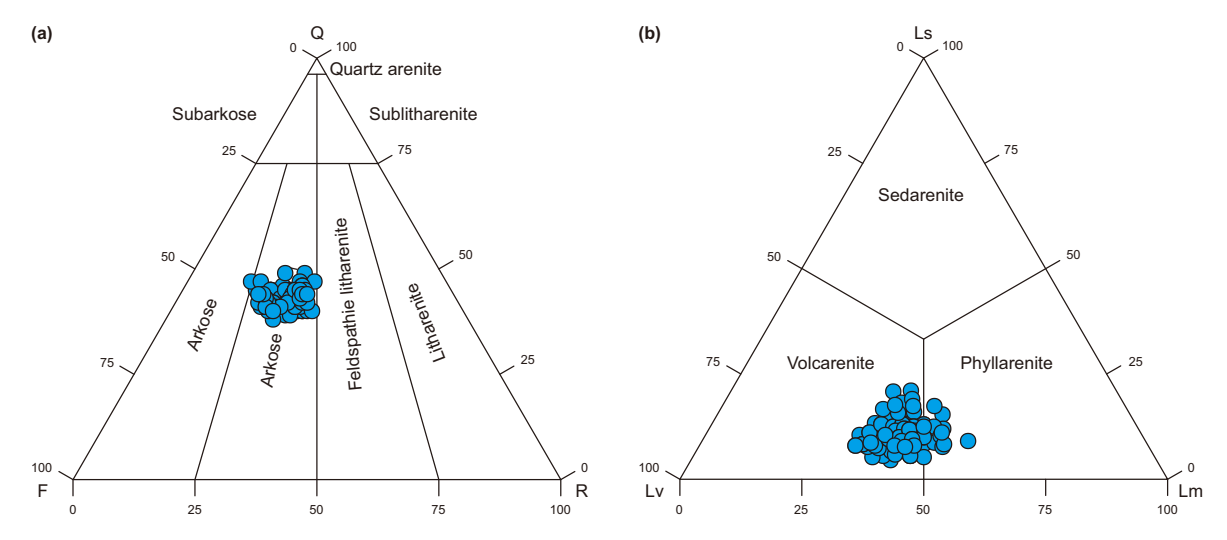


Fig. 2. (a) The triangular diagram of the minerals compositions of the sandstones. (b) The triangular diagram of rock fragments compositions of the sandstones.

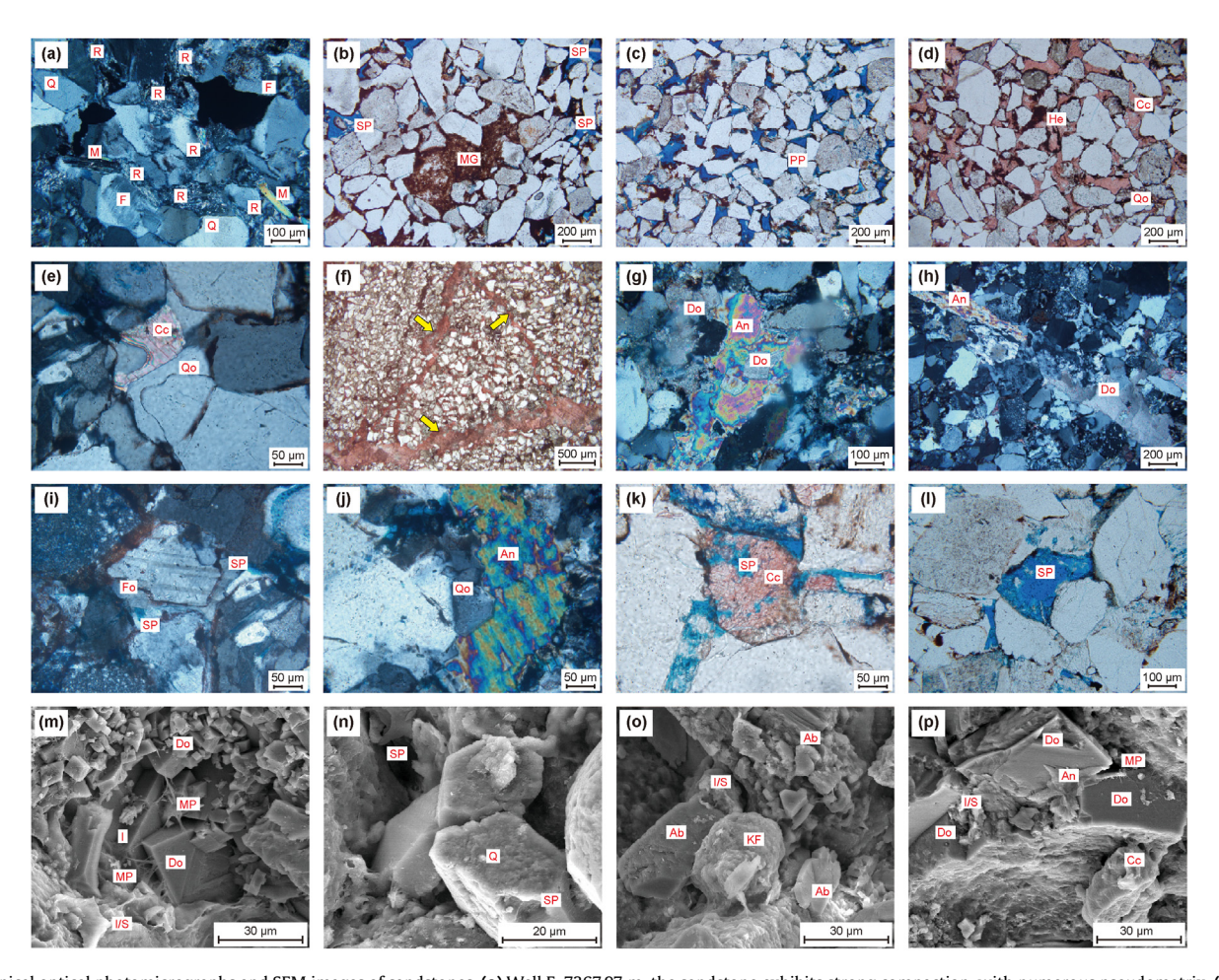


Fig. 3. Typical optical photomicrographs and SEM images of sandstones. **(a)** Well E, 7367.97 m, the sandstone exhibits strong compaction, with numerous pseudomatrix. **(b)** Well E, 7213.02 m, the mud gravel deforms strongly, resulting in local densification. **(c)** Well E, 7223.8 m, the sandstone exhibits medium compaction, with numerous primary pores. **(d)** Well A, 6927 m, the sandstone is tightly cemented by calcite. **(e)** Well B, 7027.47 m, the medium-coarse xenomorphic granular calcite submerges quartz overgrowth. **(f)** Well B, 7080.7 m, fractures are completely filled by calcite. **(g)** Well C, 6956.38 m, the medium-coarse xenomorphic granular anhydrite submerges dolomite. **(h)** Well B, 6975.5 m, fractures are completely filled by dolomite and anhydrite. **(i)** Well B, 7027.48 m, the feldspar overgrowth is dissolved locally. **(j)** Well B, 7027.48 m, the formation of anhydrite is after the Il-quartz overgrowth. **(k)** Well B, 7027.48 m, the calcite is dissolved locally. **(l)** Well B, 6918.5 m, moldic pore and residual grain skeleton. **(m)** Well E, 7221.65 m, the hairlike illite covers the dolomite. **(n)** Well E, 7215.87 m, the quartz is locally dissolved. **(o)** Well D, 7223.14 m, the K-feldspar is dissolved locally. **(p)** Well E, 7223.14 m, the anhydrite covers the dolomite, and the calcite is dissolved locally. Abbreviation: Q: Quartz, F: Feldspar, RF: Rock fragment, MG: Mud gravel, He: Hematite, Cc: Calcite, Qo: Quartz overgrowth, Do: Dolomite, An: Anhydrite, Fo: Feldspar overgrowth, I: Illite, I/S: Illite/smectite, Ab: Albite, KF: K-feldspar, PP: Primary pore, SP: Secondary pore, MP: Micropore.

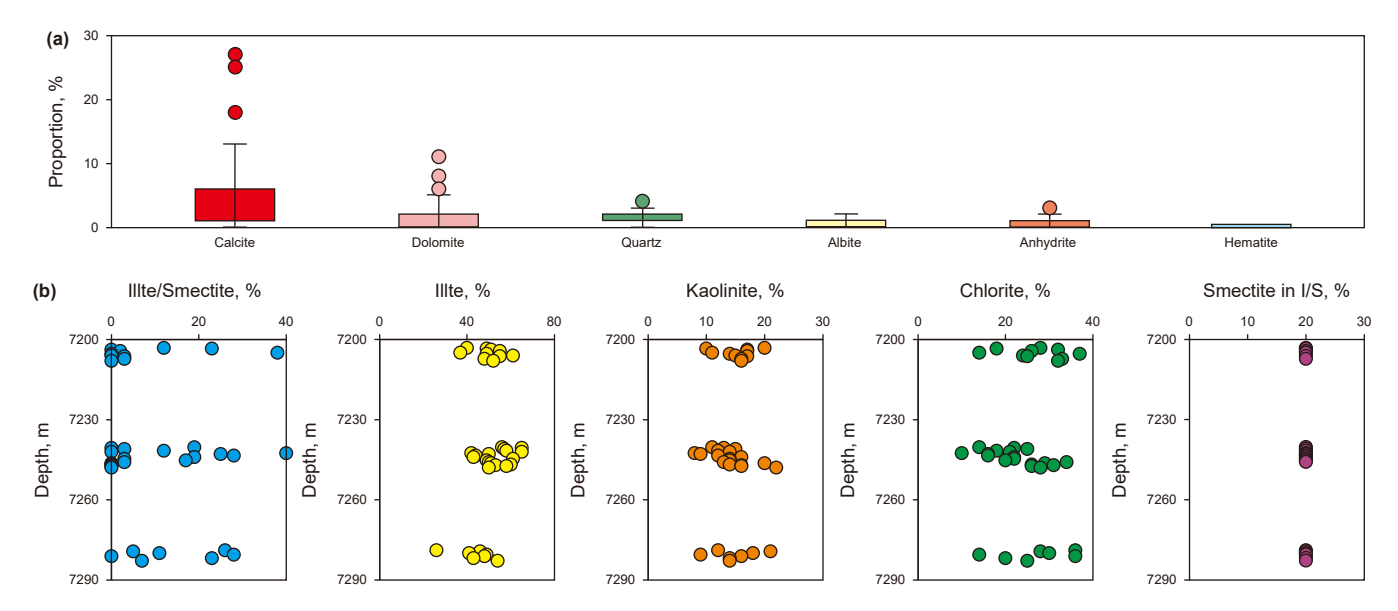


Fig. 4. (a) Box diagram of the content of main authigenic minerals. (b) XRD analysis of the content of clay minerals.

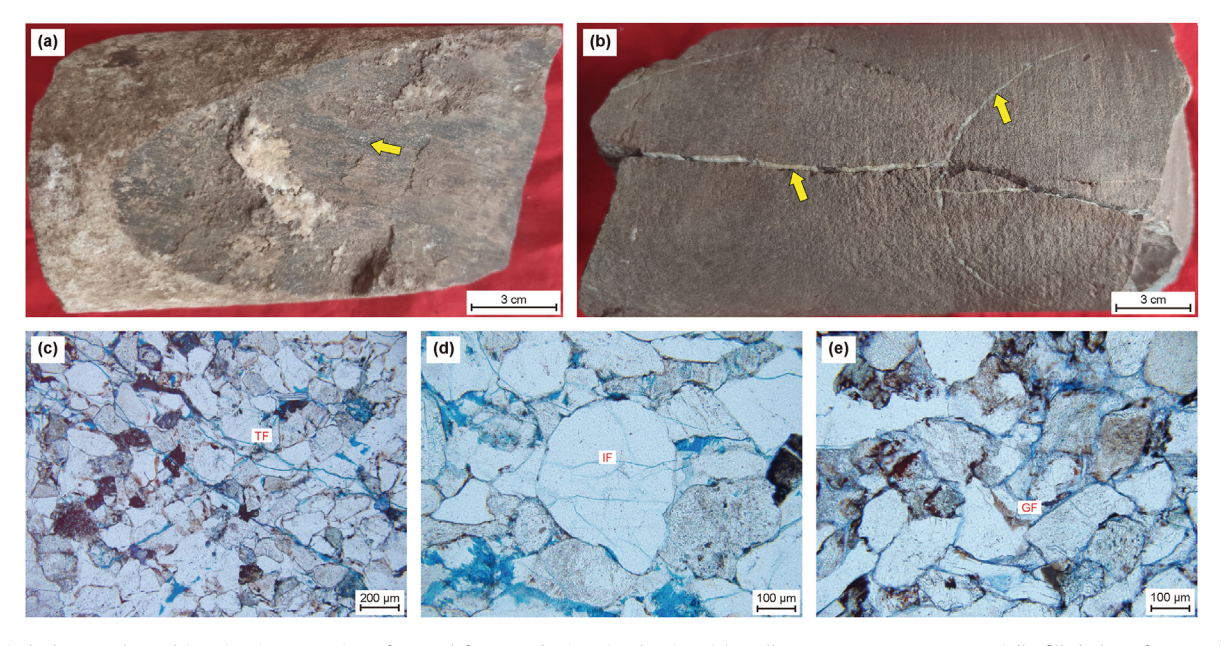


Fig. 5. Typical photographs and imaging interpretation of natural fractures by imaging logging. **(a)** Well B, 6878.94–6879.1 m, partially filled shear fracture. **(b)** Well B, 7029.92–7030.1 m, completely filled tensile fractures. **(c)** Well B, 7027.48 m, transgranular fractures. **(d)** Well F, 7204.16 m, intragranular fractures. **(e)** Well B, 6930.9 m, grain boundary fractures. Abbreviation: TF: Transgranular fracture; IF: Intragranular fracture; GF: Grain boundary fracture.

and (p)). After grains and cements are dissolved, intragranular dissolved pore, dissolution enlarged pore, mold pore are developed, with the rest of grain skeleton and hematite coating (Fig. 3(1)). Partial secondary pores are filled by calcite, dolomite and anhydrite. Due to the dissolution of quartz and feldspar, it can be inferred that the diagenetic environment undergoes an acid—alkaline transition (Li et al., 2018).

4.3. Natural fracture characteristics

Natural fractures are generally developed. It can be divided into tectonic fracture, diagenetic fracture and overpressure-related fracture (Zeng et al., 2023). Tectonic fracture is the most important type. They are mainly high-angle and near-vertical shear

fractures (Fig. 5(a)), followed by tensile fractures (Fig. 5(b)). They are mainly filled by calcite, dolomite and anhydrite (Fig. 3(e) and (h)). Microfractures are transgranular fractures (Fig. 5(c)), intragranular fractures (Fig. 5(d)), and grain boundary fractures (Fig. 5(e)) (Zeng et al., 2023). Microfractures serve as important reservoir space, and connect pores to form fracture-pore network, thus improving reservoir quality (Lai et al., 2022).

Different lithology is corresponding to different fracture linear density, among which the fractures in very fine sandstone are the most developed, with a value of 1.7 m^{-1} (Fig. 6(a)). With the increase of thickness of single sand layer, the fracture linear density decreases gradually (Fig. 6(b)). The imaging logging interpretation show that the fracture linear density of well C, E, F is 0.37, 0.18, 0.59 m⁻¹ respectively. Fractures of the K_1bs^2 mainly exhibit the

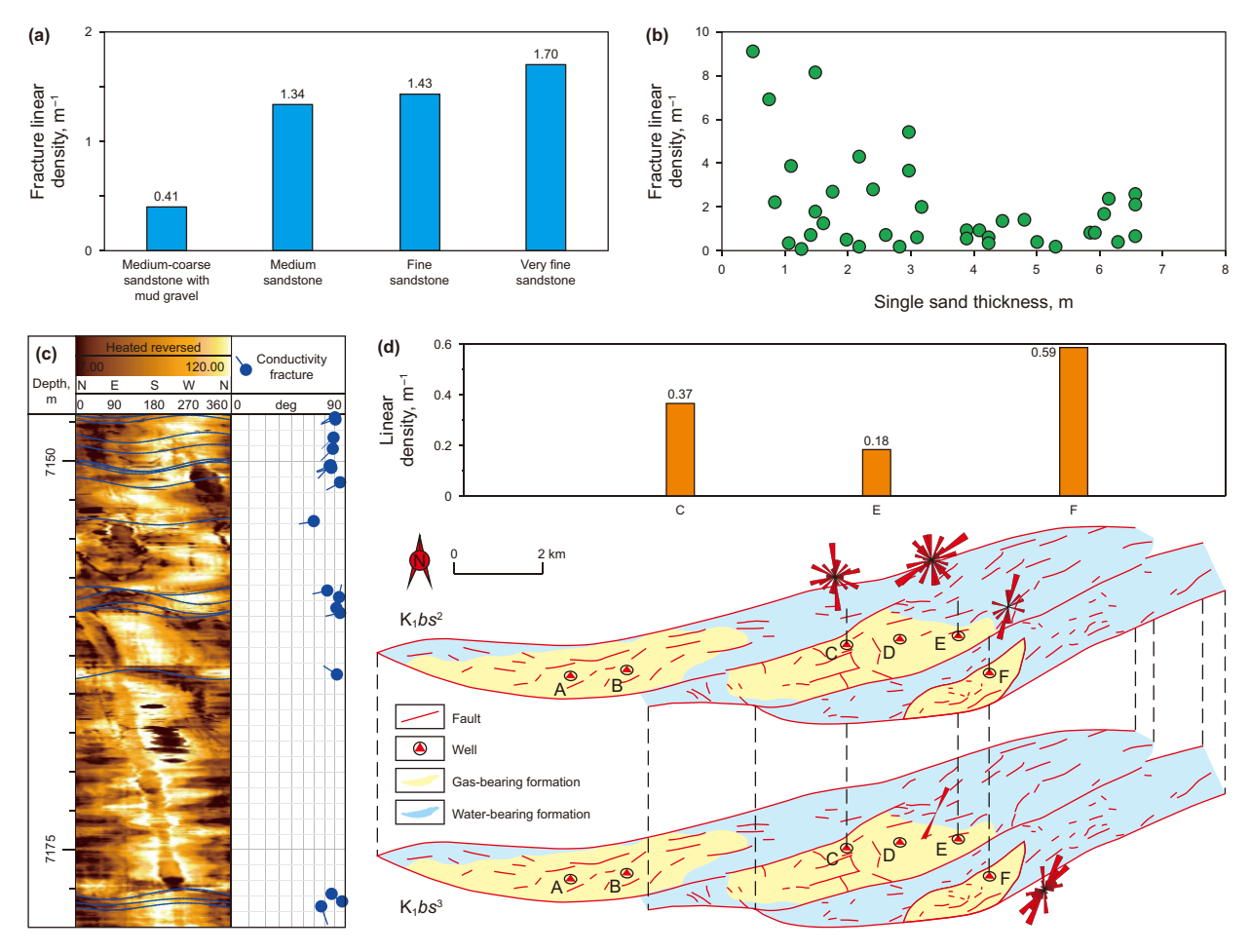


Fig. 6. (a) The histogram of fracture linear density in different lithology. (b) The scatter plot of fracture linear density corresponding to single sand thickness. (c) The imaging logs interpretation of fractures. (d) The imaging logs interpretation of the development of fractures.

N–S, NNE–SSW, NEE–SWW, NWW–SEE strikes, while that of the K_1bs^3 mainly show the NNE–SSW strikes (Fig. 6(c) and (d)).

4.4. Pore characteristic

The types of pores include primary intergranular pores, secondary dissolution pores, micropores and micro-fractures in thin section (Table 1). The contents of primary intergranular pores are 0%–4.67% (average 1.39%) (Table 1). They are distributed between detrital grains and usually exhibit regular angular. Secondary dissolution pores have contents of 0%–4% (average 1.37%) (Table 1). They generally exhibit various types, such as intergranular dissolution pores, intragranular dissolution pores, moldic pores. Secondary dissolution pores are usually in irregular shape, and the edges are harbor like. Micropores mostly occur in authigenic clay minerals in the SEM (Fig. 3(m)). Generally, in thin section, micropores, with pore size <0.5 μ m, are hardly observed under the conventional optical microscope with the resolution 1.0 μ m.

For samples before centrifugation, the T_2 spectrum presents double peaks, signifying complex pore structure (Fig. 7(a)–(f)). Pore radius ranges from 0.001 to 10 μ m, mainly concentrated in 0.01–0.1 μ m (Fig. 7(g)). The average pore radius (r) is between 0.06 and 1.23 μ m, with an average of 0.31 μ m (Table 2). The medium pore radius (r_M) ranges from 0.03 to 0.22 μ m, with an average of

0.05 μm (Table 2). The geometric mean of pore radius ($r_{\rm G}$) is within the range of 0.02–0.19 μm. with an average of 0.06 μm (Table 2). The pore radius corresponding to the peak position of the T2 spectrum ($r_{\rm P}$) is within the range of 0.02–2.51 μm, with an average of 0.24 μm (Table 2). The above parameters all indicate the development of nano-scaled pores. The kurtosis ($K_{\rm G}$) is within the range of –1.84 to 0.01, with an average of –0.93 (Table 2), suggesting a relatively uniform of pore size distribution. The skewness ($S_{\rm K}$) ranges from 0.05 to 1.03, with an average of 0.66 (Table 2), reflecting a tendency of smaller pore size distribution. The sorting coefficient ($S_{\rm P}$) falls in the range of 0.03–0.16, with an average of 0.10 (Table 2), indicating a relatively uniform of pore structure. The coefficient of variation (C) is between 0.03 and 1.96, with an average of 0.52 (Table 2), demonstrating a deficient pore structure.

The changes of the T_2 spectrum before and after centrifugation show that the bound water is mainly concentrated in small pores (Fig. 7(a)–(f)). Accordingly, most large pores are corresponding to the movable water, which can be displaced by gas during natural gas charging. The bound water saturation (S_B) has the content of 27.21%–80.32%, with an average of 55.61% (Table 2). The gas saturation (S_G) ranges from 19.68% to 72.79%, with an average of 44.39% (Table 2). The gas volume (V_G) is between 0.17 and 1.70 cm³, with an average of 0.58 cm³ (Table 2). Different pore structure results in different gas saturation. With the increase of pore size, the S_B

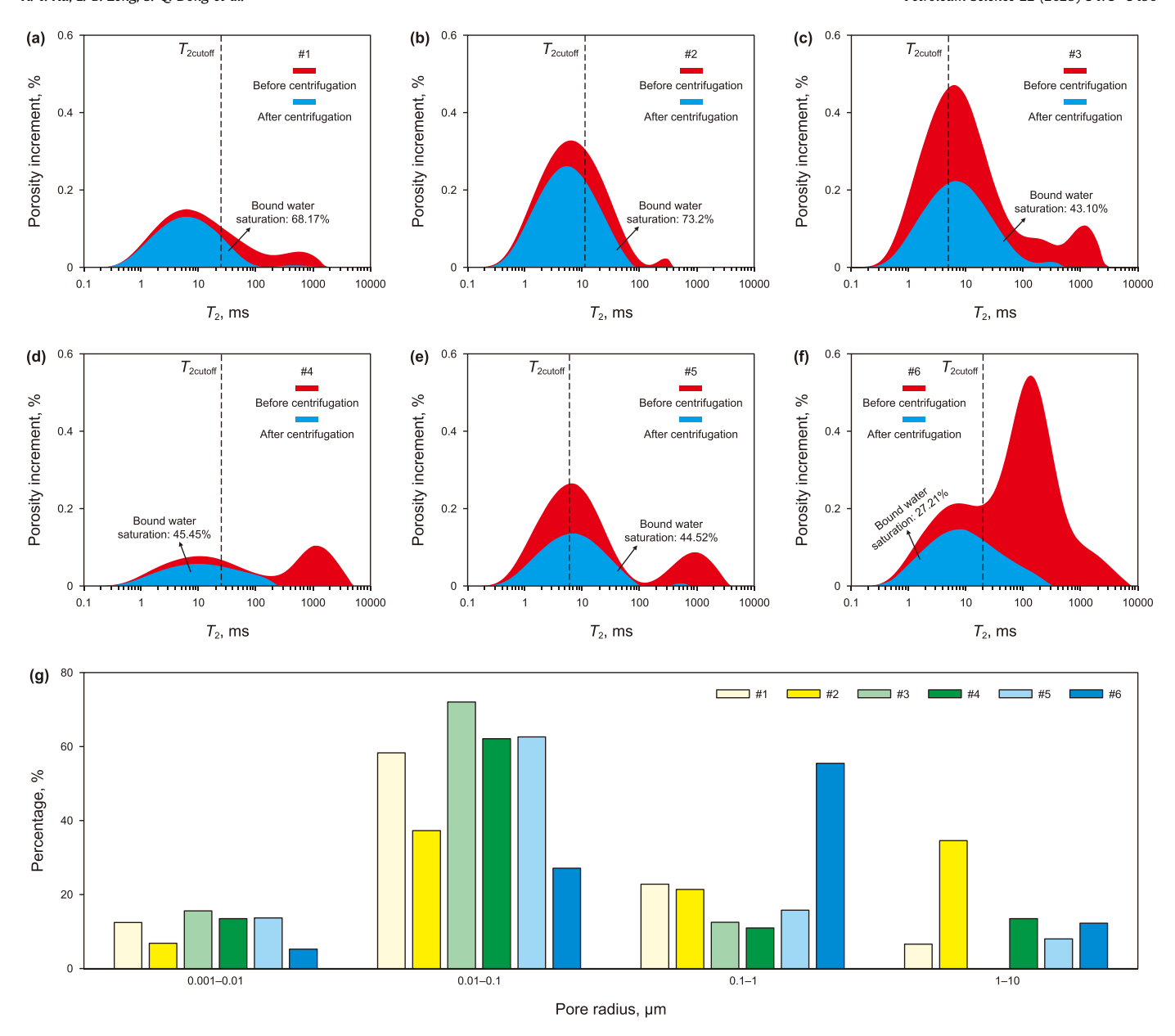


Fig. 7. (a)—(f) The T_2 spectrum for the samples #1, #2, #3, #4, #5, #6. (g) The histogram of pore size distribution.

decreases gradually. Accordingly, sandstones with better porosity and permeability are always corresponding to lower S_B , higher S_G and larger V_G .

4.5. Reservoir quality

Core-measured porosity ranges from 0.90% to 11.63% (average 5.90%), and core-measured permeability ranges from 0.0067 \times 10^{-3} to $27.5 \times 10^{-3}~\mu m^2$ (average $1.93 \times 10^{-3}~\mu m^2$) (Fig. 8(a)). Core-measured physical properties show the strong heterogeneity in reservoir quality. 39.35% of the sandstones show extremely low porosity and extremely low permeability, 47.10% of the sandstones show extremely low porosity and low permeability, 9.68% of the sandstones show low porosity and low permeability, 1.29% of the sandstones show extremely low porosity and medium permeability, 2.58% of the sandstones show low porosity and medium permeability (Fig. 8(a)). In addition, 18.71% of the sandstones show abnormally low porosity and abnormally high permeability, which

deviate from the overall relationship between porosity and permeability. On the whole, the sandstones also show a positive linear correlation between the core-measured porosity and the thin section-measured porosity (Fig. 8(b)).

4.6. Formation sequences of diagenesis and tectonic fractures

The smectite in I/S accounts 20% (Fig. 4(b)). Bottom hole temperature is between 140 and 160 °C. It can be inferred that the reservoir is in meso-diagenetic A stage (Wang et al., 2022). The reservoir has undergone syndiagenesis, eodiagenesis, epidiagenesis, eodiagenesis and mesodiagenesis A (Li et al., 2018). In addition, previous studies have shown that tectonic fractures can be categorized into three stages: the nearly E–W striking fractures during the late Yanshan period, the nearly N–S striking fractures during the middle Himalayan period, and a few nearly E–W striking fractures along with the predominant nearly N–S striking

 Table 2

 Pore structure parameters obtained from the NMR experiments.

Well	Depth, m	Diagenetic facies	Porosity, %	Permeability, 10 ⁻³ μm ²	Pore volume, cm ³	r, μm	r _M , μm	r _G , μm	r _V , μm	K _G	S _K	S _P	С	S _B ,	S _G ,	V _G , cm ³
В	6878.94	A	7.1	0.186	1.620	0.224	0.054	0.067	0.035	-1.659	0.161	0.127	0.567	37.68	62.32	1.010
В	6920.69	В	4.3	0.074	1.200	0.144	0.034	0.042	0.029	-0.845	0.793	0.086	0.598	64.52	35.48	0.426
В	6922.66	C	2.5	0.080	0.500	0.302	0.050	0.065	0.029	-1.207	0.504	0.040	0.132	50.00	50.00	0.250
В	6933.75	В	4.6	0.105	1.240	0.181	0.029	0.039	0.024	-0.662	0.906	0.096	0.528	66.89	33.11	0.411
E	7212.32	Α	6.9	0.222	1.500	0.210	0.057	0.072	0.035	-1.842	0.050	0.122	0.580	38.41	61.59	0.924
E	7216.23	Α	8.0	0.670	2.240	0.161	0.041	0.051	0.024	-1.336	0.461	0.156	0.971	43.84	56.16	1.258
E	7224.14	В	5.6	0.106	1.490	0.228	0.038	0.053	0.024	-1.021	0.595	0.101	0.440	67.96	32.04	0.477
E	7290.98	В	5.3	0.174	1.430	0.184	0.036	0.050	0.024	-0.995	0.580	0.100	0.539	62.96	37.04	0.530
E	7291.57	В	3.2	0.069	0.870	0.256	0.039	0.053	0.024	-0.959	0.654	0.055	0.213	68.17	31.83	0.277
E	7291.78	В	4.6	0.044	1.030	0.084	0.028	0.030	0.029	-0.800	0.931	0.115	1.368	77.18	22.82	0.235
E	7292.21	В	4.9	0.056	1.000	0.061	0.027	0.030	0.029	-0.783	0.927	0.120	1.960	73.20	26.80	0.268
E	7292.47	В	4.6	0.075	1.050	0.234	0.046	0.063	0.029	-1.396	0.316	0.082	0.348	66.29	33.71	0.354
E	7292.90	C	2.8	0.128	0.770	0.246	0.026	0.031	0.020	-0.540	1.029	0.074	0.302	64.78	35.22	0.271
E	7296.00	В	4.0	0.035	0.820	0.138	0.029	0.034	0.024	-0.904	0.830	0.086	0.625	49.05	50.95	0.418
E	7296.77	В	5.7	0.049	1.090	0.138	0.039	0.046	0.029	-1.256	0.550	0.113	0.821	55.42	44.58	0.486
E	7298.01	В	4.2	0.041	0.880	0.137	0.027	0.024	2.508	-0.705	0.949	0.079	0.576	80.32	19.68	0.173
F	7203.11	C	2.8	0.040	0.730	0.548	0.050	0.083	0.024	-0.931	0.470	0.040	0.074	43.82	56.18	0.410
F	7204.96	В	4.3	0.071	1.120	0.493	0.033	0.055	0.024	-0.519	0.916	0.087	0.177	44.52	55.48	0.621
F	7206.11	Α	6.8	0.087	1.790	0.396	0.037	0.058	0.029	-0.818	0.734	0.130	0.327	55.31	44.69	0.800
F	7207.99	Α	8.8	0.338	2.340	0.663	0.222	0.186	0.360	0.014	0.916	0.158	0.238	27.21	72.79	1.703
F	7243.38	C	2.6	0.046	0.660	1.225	0.151	0.030	2.065	-1.109	0.099	0.032	0.026	45.45	54.55	0.360
F	7296.30	В	4.3	0.055	1.100	0.445	0.040	0.062	0.024	-0.723	0.758	0.076	0.171	52.84	47.16	0.519
F	7247.37	Α	7.6	0.082	1.910	0.330	0.032	0.048	0.029	-0.481	0.957	0.154	0.467	43.10	56.90	1.087

Note: r = Average pore radius, μm ; $r_M = \text{Medium pore radius}$, μm ; $r_G = \text{Geometric mean of pore radius}$, μm ; $r_V = \text{Pore radius corresponding to the peak position of the } T_2$ spectrum, μm ; $K_G = \text{Kurtosis}$; $S_K = \text{Skewness}$; $S_P = \text{Sorting coefficient}$; C = Coefficient of variation (S_P/r); $S_B = \text{Bound water saturation}$, %; $S_G = \text{Gas saturation}$, %; $V_G = \text{Gas volume}$, C = Coefficient of variation (C_P/r); $C_R = \text{Coefficient}$ of variation (C_R/r); C_R/r of variati

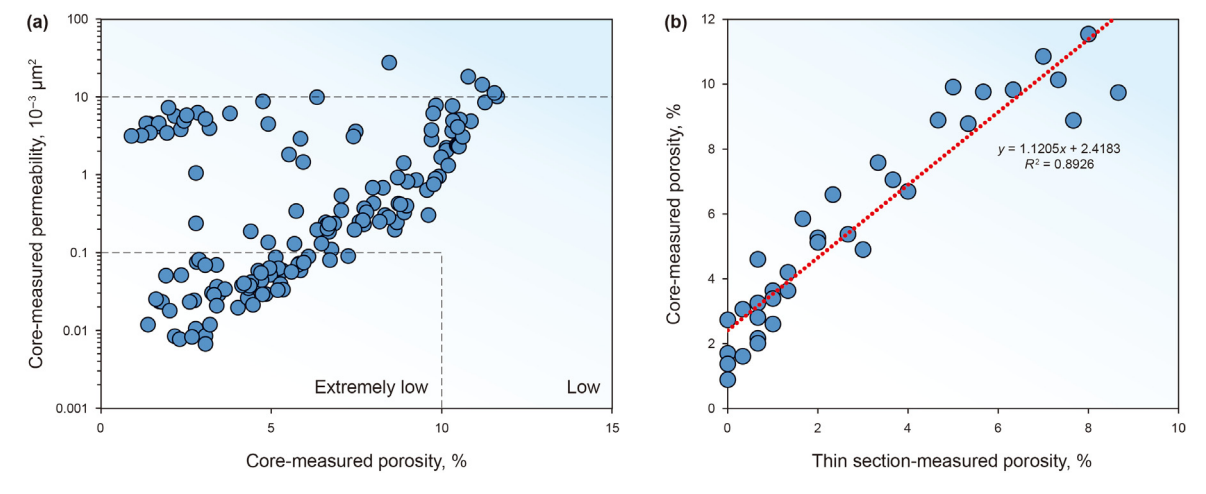


Fig. 8. (a) The scatter diagram between core-measured porosity and core-measured permeability. (b) The scatter diagram between thin section-measured porosity and core-measured porosity.

fractures in the late Himalayan period (Zeng, 2004; Wei et al., 2020).

Combined with the symbiosis/emplacement relationship between different diagenetic minerals observed under the microscope, the diagenetic sequence is calibrated by carbon and oxygen isotope and micro thermometry of inclusions of typical minerals (Fig. 9).

- (1) Continuous burial compaction and strong tectonic compression in the late Himalayan period.
- (2) For the sandstone tightly cemented by carbonate cements, it can be seen that only hematite coating remains after the grain are completely dissolved (Fig. 3(d)). It can be inferred that the formation of hematite coating is earlier than the dissolution. Meanwhile, compared with the hematite coating deformed by compaction in Fig. 3(l), this hematite coating

shows slighter deformation. There is no obvious deformation of the grains, indicating that this sandstone has not undergone large-scale compaction. In addition, partial quartz and feldspar develop overgrowth. Therefore, it can be inferred that the dissolution occurs in epidiagenesis. The formation of Hematite coating is earlier than the epidiagenesis. After the epidiagenesis, the sandstone undergoes the I-quartz/feldspar overgrowth. Subsequently, the sandstone is tightly cemented by carbonate cements.

- (3) The medium-coarse xenomorphic granular calcite covers the quartz/feldspar overgrowth, indicating that its formation is relatively later.
- (4) The anhydrite covers II-quartz overgrowth and dolomite, indicating that its formation is relatively later.
- (5) The hairlike illite covers dolomite, indicating that its formation is relatively later.

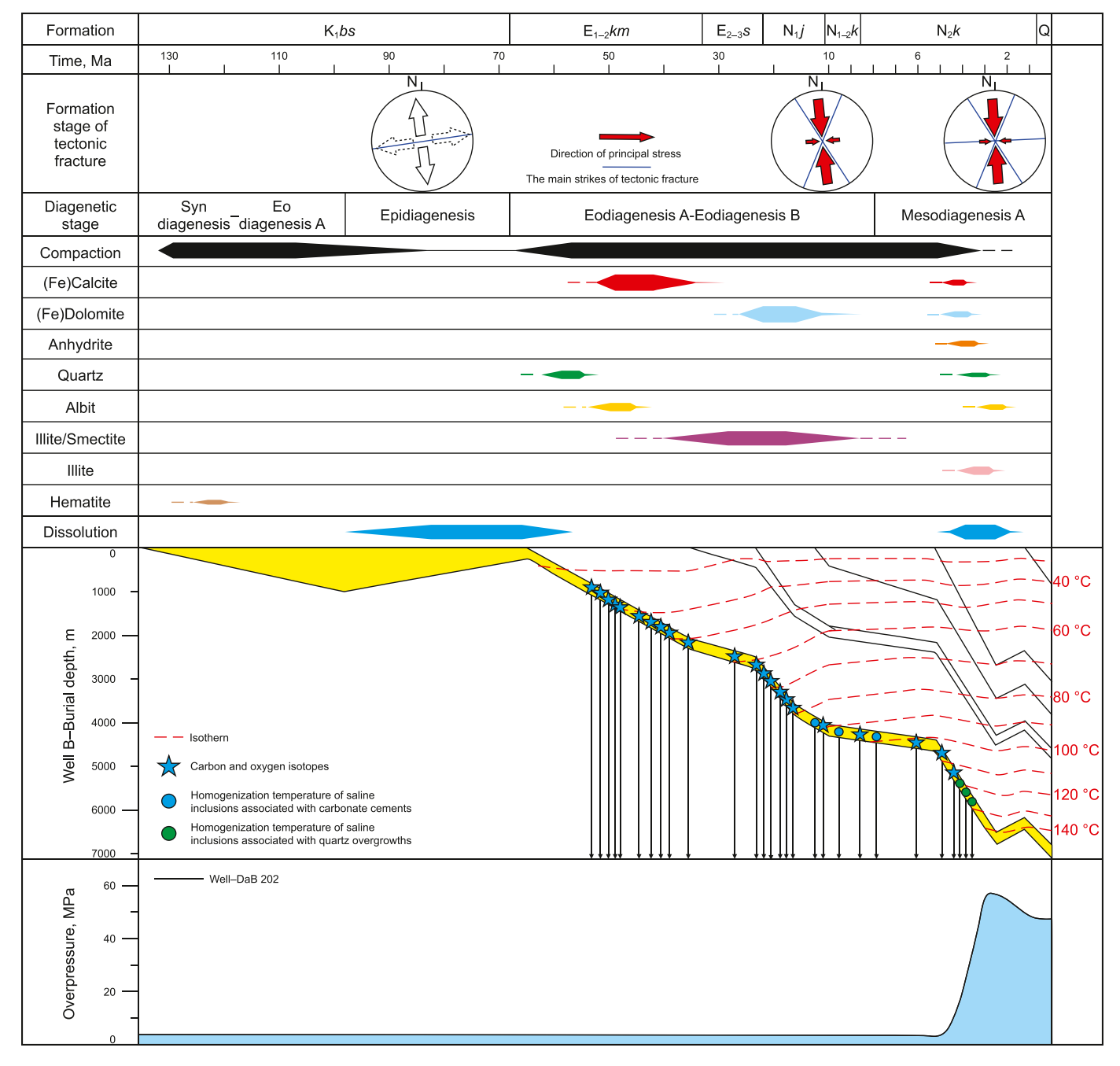


Fig. 9. The evolution of thermal history, burial history, diagenetic sequence, tectonic fracture, and overpressure (modified after Guo et al., 2016a; Wei et al., 2020; Yang et al., 2024) (The data of carbon and oxygen isotopes and homogenization temperature of inclusions are from Zhang (2019) and Yang (2011)).

5. Discussion

5.1. Diagenetic facies typing and high-quality reservoir type

Fig. 10(a) shows that the COPL ranges from 13.70% to 35.05% (average 29.87%), and the CEPL ranges from 1.95% to 23.30% (average 6.15%). It can be seen that compaction and cementation have obviously different effects on reservoir quality. Porosity loss is mainly dominated by compaction, locally by cementation. Based on texture and composition of detrital grains, authigenic minerals, diagenetic type and intensity, pore structure, core-measured physical properties and gas saturation, sandstones are divided

into three diagenetic facies: diagenetic facies A, diagenetic facies B, diagenetic facies C (Fig. 10).

Diagenetic facies A: Rigid grains are common, while ductile grains and mud gravel can be seen locally. Authigenic minerals include carbonate cements, quartz/feldspar overgrowth, anhydrite, authigenic clay minerals, hematite. Pore types are dominated by primary pores, followed by secondary pores. The r ranges from 0.161 to 0.663 μ m (average 0.331 μ m) (Table 2). The $r_{\rm M}$ is between 0.032 and 0.222 μ m (average 0.074 μ m) (Table 2). The $r_{\rm G}$ is within the range of 0.048–0.186 μ m (average 0.080 μ m) (Table 2). The $r_{\rm V}$ falls within the range of 0.024–0.360 μ m (average 0.085 μ m) (Table 2). The COPL ranges from 28.13% to 32.75% (average 29.57%),

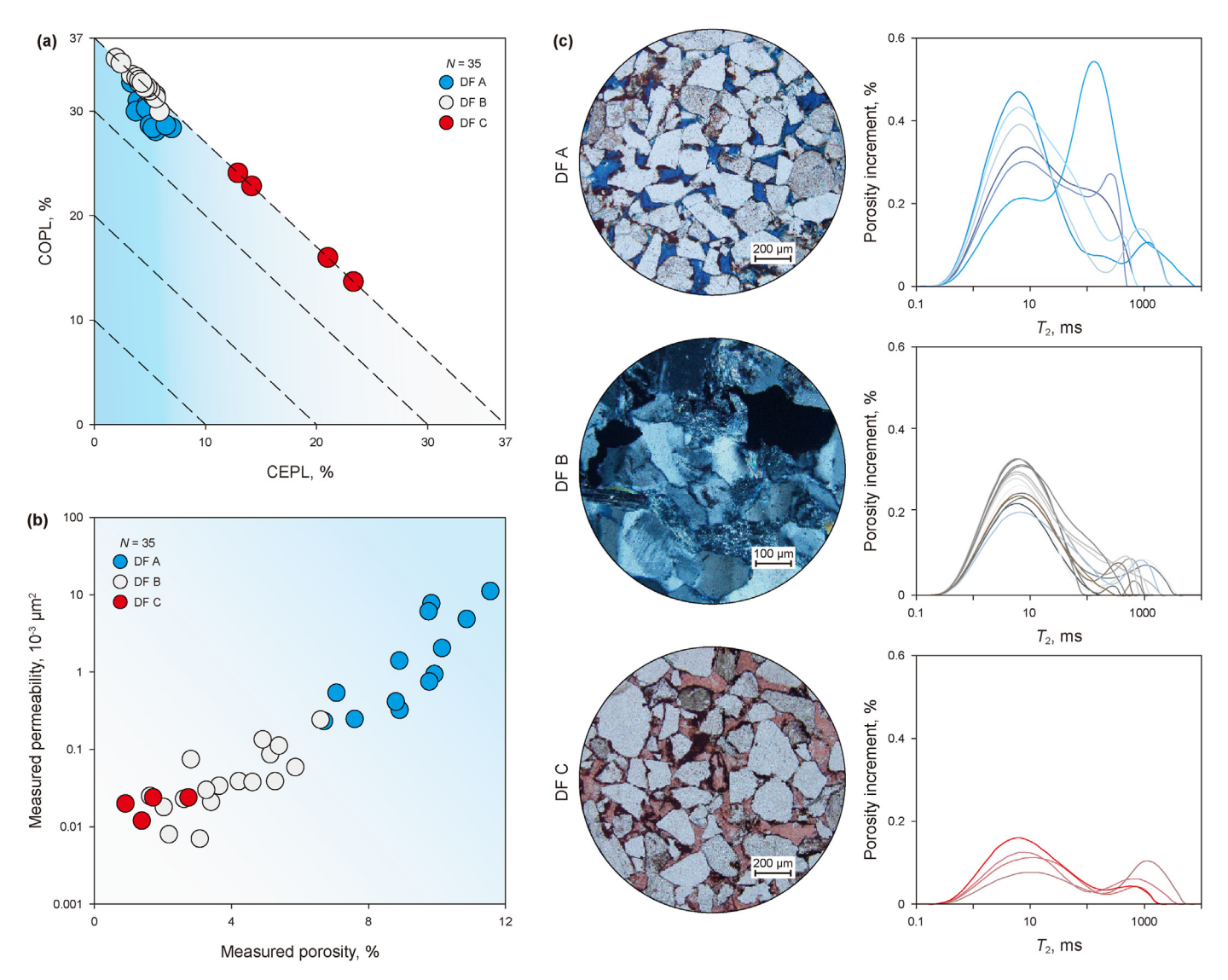


Fig. 10. (a) The intersection diagram of COPL and CEPL. **(b)** The intersection diagram of measured porosity and measured permeability. **(c)** Typical micrographs, T_2 spectrum for different diagenetic facies.

and the CEPL ranges from 3.36% to 6.92% (average 5.02%). Coremeasured porosity ranges from 6.70% to 11.55% (average 9.21%) (Fig. 10(b)). Pore volume ranges from 1.50 to 2.34 cm³ (average 1.90 cm³) (Table 2). The S_G ranges from 44.690% to 72.790% (average 59.075%) (Table 2). The V_G ranges from 0.800 to 1.703 cm³ (average 1.130 cm³) (Table 2). This sandstone generally exhibits medium compaction, weak-medium cementation, strong dissolution. The good physical properties and gas bearing characteristics make diagenetic facies A the high-quality reservoir of ultra-deep tight gas sandstone.

Diagenetic facies B: Ductile grains show high content. Strongly deformed matrix, pseudomatrix, mica and mud gravel are also common. Cements and pores are only sporadically visible. The r ranges from 0.061 to 0.493 μ m (average 0.210 μ m) (Table 2). The $r_{\rm M}$ is between 0.027 and 0.046 μ m (average 0.034 μ m) (Table 2). The $r_{\rm G}$ is within the range of 0.024–2.508 μ m (average 0.045 μ m) (Table 2). The $r_{\rm V}$ falls within the range of 0.024–0.360 μ m (average 0.217 μ m) (Table 2). The COPL ranges from 29.99% to 35.05% (average 32.45%), and the CEPL ranges from 1.95% to 5.84% (average 4.38%) (Fig. 10(a)). Core-measured porosity is generally poor and ranges from 1.62% to 6.6% (average 3.78%) (Fig. 10(b)). The pore volume ranges from

0.820 to 1.490 cm³ (average 1.102 cm³) (Table 2). The S_G ranges from 19.680% to 55.480% (average 36.206%) (Table 2). The V_G ranges from 0.173 to 0.621 cm³ (average 0.400 cm³) (Table 2). This sandstone generally exhibits strong compaction, weak cementation, weak dissolution. Strong compaction is the main cause for densification. The poor physical properties and gas bearing characteristics make diagenetic facies B tend to be the barrier for hydrocarbon charging.

Diagenetic facies C: The sandstone is tightly cemented by carbonate cements, with almost no pores visible. The r ranges from 0.25 to 1.23 µm (average 0.58 µm) (Table 2). The $r_{\rm M}$ is between 0.03 and 0.15 µm (average 0.07 µm) (Table 2). The $r_{\rm G}$ is within the range of 0.03–0.08 µm (average 0.05 µm) (Table 2). The $r_{\rm V}$ falls within the range of 0.02–2.07 µm (average 0.53 µm) (Table 2). The COPL ranges from 13.70% to 24.10% (average 19.16%), and the CEPL ranges from 12.90% to 23.30% (average 17.84%) (Fig. 10(a)). Core-measured porosity ranges from 0.90% to 2.74% (average 1.68%) (Fig. 10(b)). The pore volume ranges from 0.500 to 0.770 cm³ (average 0.665 cm³) (Table 2). The $S_{\rm G}$ ranges from 35.220% to 56.180% (average 48.988%) (Table 2). The $V_{\rm G}$ ranges from 0.250 to 0.410 cm³ (average 0.323 cm³) (Table 2). This sandstone generally exhibits weak compaction, strong cementation, weak dissolution. Strong

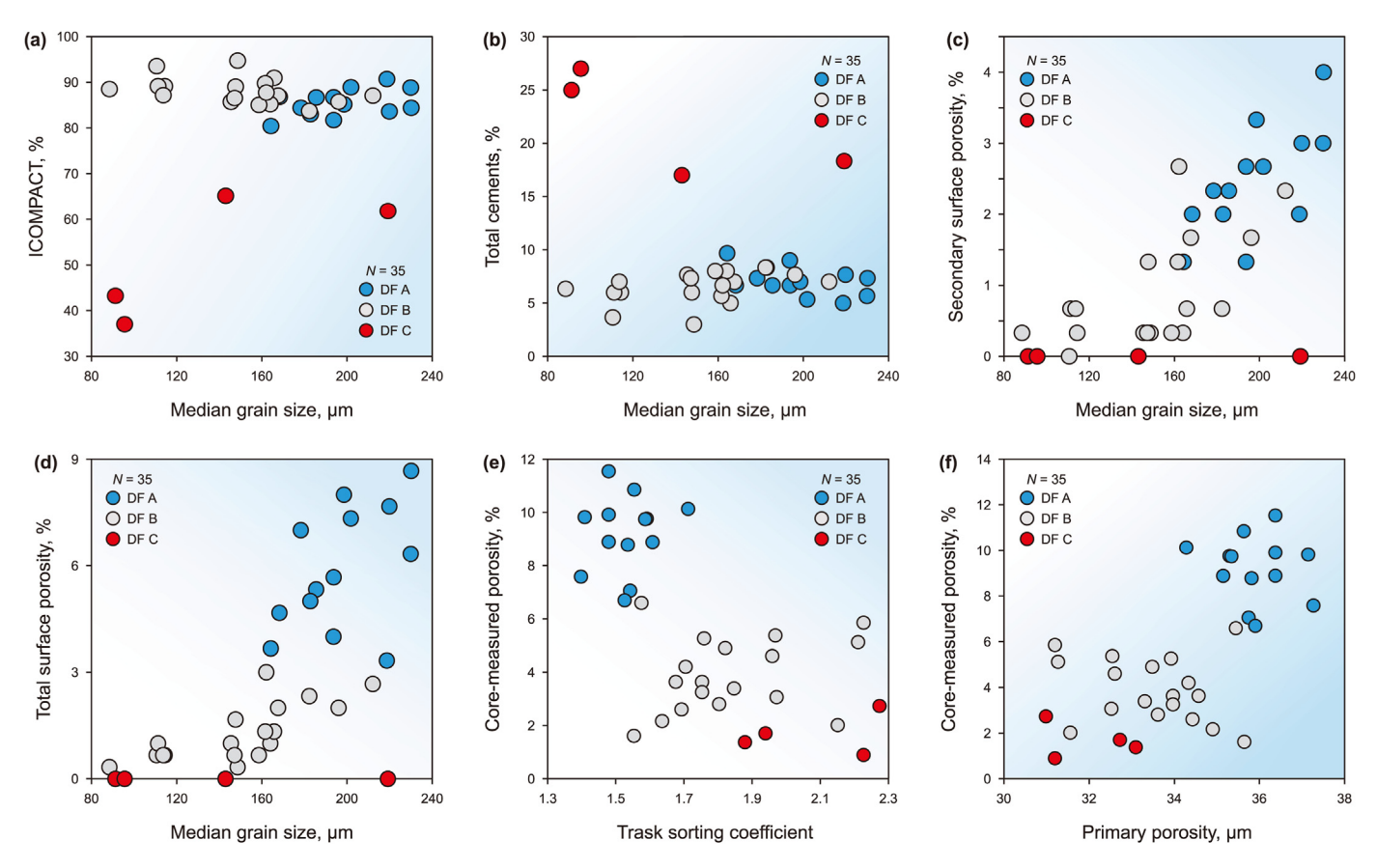


Fig. 11. (a) The scatter diagram of median size and ICOMPACT. (b) The scatter diagram of median size and total cements. (c) The scatter diagram of median size and secondary plane porosity. (d) The scatter diagram of median size and total plane porosity. (e) The scatter diagram of So and core-measured porosity. (f) The scatter diagram of primary porosity and core-measured porosity.

cementation is responsible for densification. The extremely poor physical properties and gas bearing characteristics show diagenetic facies C is the barrier for hydrocarbon charging.

5.2. Control factors on reservoir heterogeneity

5.2.1. Sedimentation

Sedimentation provides the material basis for reservoir development (Zeng et al., 2016a). Sedimentary hydrodynamic force controls the texture and composition of detrital grains (Henares et al., 2016; Yang et al., 2022; Yan et al., 2023). Differential distribution of detrital grains results in different distribution of reservoir. Subsequently, differential diagenesis leads to dynamic evolution of reservoir quality (Luo et al., 2020; Luo et al., 2023a; Cao et al., 2024a).

5.2.1.1. Texture of detrital grains. With increases of median grain size, the COPL gradually decreases (Fig. 11(a)), while the total cements (Fig. 11(b)), secondary surface pores (Fig. 11(c)) and total surface porosity (Fig. 11(d)) gradually increase. It is illustrated that diagenetic intensity is related with grain size. Accordingly, different diagenetic facies show different characteristics in medium grains, S_0 , and primary porosity (Fig. 11(e) and (f)). The median grain size of diagenetic facies A, B and C are 164.26–230.16 μ m (average 197.39 μ m), 88.45–212.14 μ m (149.50 μ m), 91.23–219.22 μ m (137.28 μ m), respectively (Table 1). The S_0 of diagenetic facies A, B and C are 1.398–1.712 (average 1.531), 1.553–2.227 (average 1.837), 1.879–2.274 (average 2.080), respectively (Table 1). The primary porosity of diagenetic facies A, B and C are 34.285%–37.286%

(average 35.912%), 31.194%—35.656% (average 33.518%), 30.982%—33.097% (average 31.999%), respectively (Table 1). It can be seen that diagenetic facies A exhibits the best primary porosity.

Brown mud gravels are common, with grain size varying from millimeter to decimeter (Fig. 12). Enriched or sporadic mud gravels typically display elliptical, angular, and irregular shapes, predominantly occurring within the middle and lower part of the thick massive sandstone or along bedding surfaces. Mud gravels are formed when the sand and mud on the riverbank collapses and accumulates in situ, or are transported in short distance (Gao et al., 2016). Vertically, mud gravels mainly develop in the medium-fineto medium-grained sandstone, with a few in the very fine-to finegrained sandstone (Fig. 12). It is reflected that the formation of mud gravels is in a high-energy hydrodynamic environment. Microscopic characteristics show that, strong bending deformation of the mud gravel results in local densification (Fig. 3(b)). Therefore, high mud gravels content seriously reduces the reservoir quality.

5.2.1.2. Relationship between sedimentary microfacies and diagenetic facies. Variation of grain size reflects changes of sedimentary hydrodynamics laterally, and the gradual change of different sedimentary microfacies vertically (Xu et al., 2021). By clarifying the relationships between diagenetic facies and sedimentary microfacies, the controls of sedimentary microfacies on diagenetic facies are cleared.

As Fig. 12 shows, diagenetic facies A is mainly corresponding to the medium-fine-to medium-grained sandstone. It is mainly deposited in the strong hydrodynamic environment such as the lower part of the distributary channel and the upper part of the

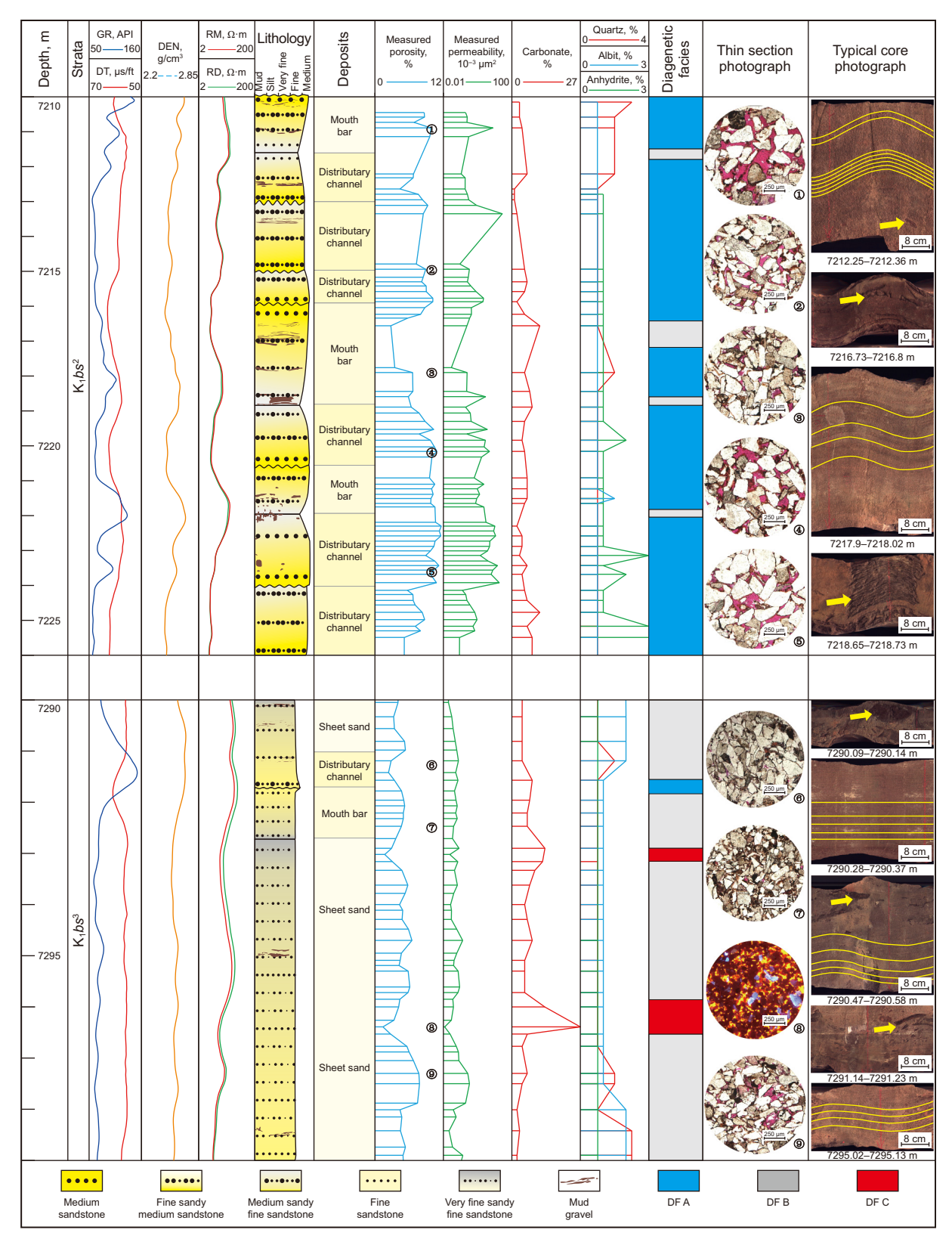


Fig. 12. Comprehensive interpretation profile of sandstone texture, porosity and permeability, sedimentary microfacies and diagenetic facies for well E (thin sections were filled with red epoxy resin).

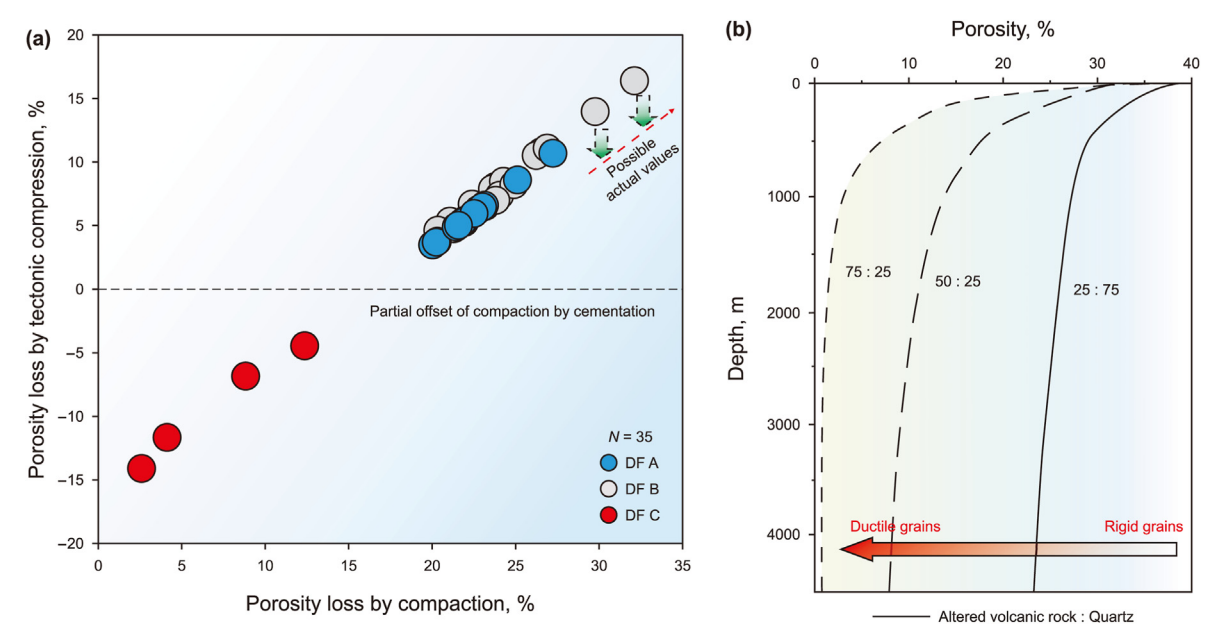


Fig. 13. (a) The scatter diagram of Φ_{Co} and Φ_{Tc} (b) The relationship between porosity and depth of sandstone with different ratio of quartz and altered volcanic rock (modified after Pittman and Larese (1991)).

mouth bar. Trough cross-bedding and plate cross-bedding are common, diagenetic facies B is mainly corresponding to very fine to fine-grained sandstone, followed by mud gravel-rich medium-grained sandstone. The generally fine grain size reflects weak sedimentary hydrodynamic. It is mainly distributed in sheet sand, and can be seen in the upper part of distributary channel or the lower part of mouth bar. Horizontal bedding, ripple bedding and block bedding can usually be seen. It is remarkable that, for partial very fine to fine-grained sandstone formed in relatively high energy environment (depth 7297.05—7297.9 m), they can also exhibit relatively good physical property, diagenetic facies C is mainly very fine to fine-grained sandstone, mainly distributed in sheet sand. The thickness is generally thin, and the distribution is limited.

5.2.2. Tectonic compression

As Fig. 13(a) shows, Φ_{CO} of diagenetic facies A, B and C are 20.02%–27.22% (average 22.32%), 20.34%–32.13% (average 24.39%), 2.58 %–12.37% (average 6.97%), respectively; Φ_{T} of diagenetic facies A, B and C are 3.49%–10.71% (average 5.79%), 4.63%–16.42% (average 8.30%), -14.09% to -4.43% (average -9.25%), respectively.

In view of significant effects of texture and composition of detrital grains on compaction intensity, and the sampling standard of the compaction simulation experiment which is only suitable for diagenetic facies A, the Φ_{CO} and Φ_{T} of diagenetic facies A is close to the actual value. In contrast, numerous ductile grains are deformed in diagenetic facies B. The rock fragments in the study area are volcanic rock fragments. As shown in Fig. 13(b), with the increase of the content of altered volcanic rock, the porosity loss by compaction increases at the same depth. Therefore, for the same burial depth, the Φ_{B} of diagenetic facies B is greater than that of diagenetic facies A. Accordingly, the actual Φ_{T} of diagenetic facies B is smaller than the theoretical values (Fig. 13(a)). For diagenetic facies C, due to diagenetic facies C densification too early, cements offset partial tectonic compression. Therefore, the Φ_{T} exhibits negative.

The relationship between the tectonic setting and reservoir quality is reflected by the difference between the Dabei 3 gas reservoir and the Keshen 24 gas reservoir. As shown in Fig. 1(b), the Keshen 24 gas reservoir is located in the north of the Kuqa

depression, close to the southern Tianshan orogenic belt, while the Dabei 3 gas reservoir is located in the south of the Kuqa depression, far away from the southern Tianshan orogenic belt. 3D pre-stack depth migration data shows that the Keshen 24 gas reservoir exhibits the pop-up structure (Fig. 14). It is formed by the N-S compression and the back thrust faults, and the interlimb angle is 130°. The Dabei 3 gas reservoir appears the gentle faulted anticline (Fig. 14). It is formed by the N–S compression, vertical compaction, and double-thrust fault (Hou et al., 2019), and the interlimb angle is 160°. The $\Phi_{\rm T}$ of diagenetic facies A ranges from 5.824% to 10.018% in the Keshen 24 gas reservoir, while that is in the range of 3.491%— 10.707% in the Dabei 3 gas reservoir (Fig. 14). Accordingly, the tectonic compression of the Dabei 3 gas reservoir is weaker than that of the Keshen 24 gas reservoir. The weak structural setting is good for porosity preservation. It is worth noting that the gas reservoirs around the Dabei 3 gas reservoir all appear the gentle faulted anticline. It is illustrated that the tectonic compression is weaker and weaker from north to south in Kuqa depression.

5.2.3. Natural fractures

Table 3 shows the core-measured physical properties of different samples. For samples with similar porosity, the permeability of fracture samples is generally 2-3 orders of magnitude higher than that of matrix samples (Fig. 15(a)). The permeability is the largest in the direction parallel to the fracture surface, while that is smaller in the direction intersecting with the fracture surface (Fig. 15(b)). Therefore, natural fractures can significantly increase the permeability of the reservoir and facilitate fluid migration. In addition, combined with Fig. 6(a) and Table 1, natural fractures tend to develop in the diagenetic facies B and C.

5.2.4. Gypsum rock

The overlying gypsum rock is composed of mudstone, gypsumsalt, dolomite, gypsum-mud, and gypsum-salt-dolomite, with the total thickness between 1025 and 2154.5 m (Fig. 16(a)). The thickness of gypsum-salt rock ranges from 210.5 to 1304 m (Fig. 16(a)). The average density of gypsum-salt and sandstone/mudstone are 1.81 and 2.59 g/cm³, respectively (Fig. 16(b)). Under the same burial

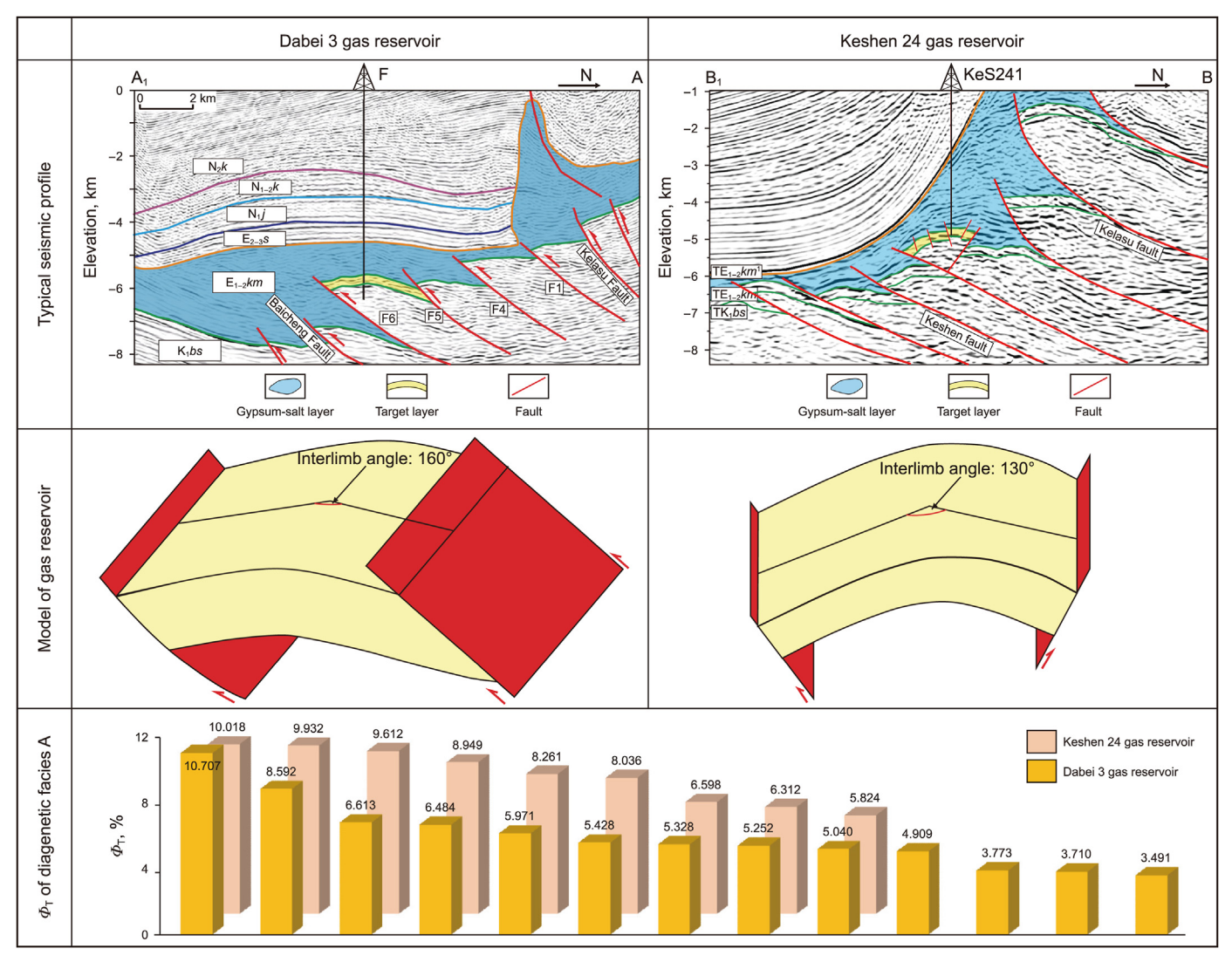


Fig. 14. The 3D pre-stack depth migration data, the tectonic model, and the $\Phi_{\rm T}$ of diagenetic facies in the Dabei 3 gas reservoir and the Keshen 24 gas reservoir.

Table 3Results of core-measured permeability for different samples.

Well	Depth, m	Lithology	Density, g/cm ³	Porosity,	Permeability,	Permeability (full diameter), 10 ⁻³ μm ²				
				%	$10^{-3} \; \mu \text{m}^2$	Vertical	Later-1	Later-2		
F	7277.77	Fine sandstone	2.49	6.34	9.930					
E	7218.89	Medium sandstone	2.50	6.35	0.195					
F	7278.55	Fine sandstone	2.52	4.91	4.470					
E	7298.90	Medium sandstone	2.54	4.91	0.135					
F	7279.92	Fine sandstone	2.54	4.76	8.710					
E	7294.29	Fine sandstone	2.55	4.74	0.029					
F	7282.75	Fine sandstone	2.58	3.07	5.210					
E	7366.76	Fine sandstone	2.59	3.07	0.009					
F	7278.96	Fine sandstone	2.60	2.34	3.820					
E	7291.42	Fine sandstone	2.61	2.36	0.051					
F	7279.17	Fine sandstone	2.60	1.98	7.260					
E	7364.98	Medium sandstone	2.62	2.02	0.018					
F	7281.55	Fine sandstone	2.63	1.70	4.570					
E	7293.02	Fine sandstone	2.63	1.71	0.024					
F	7204.45	Fine sandstone	2.58	3.00		0.061	0.114	0.021		
В	7030.94	Fine sandstone	2.63	1.38		1.110	0.243	0.222		
В	7031.71	Fine sandstone	2.58	2.99		0.355	5.230	0.259		

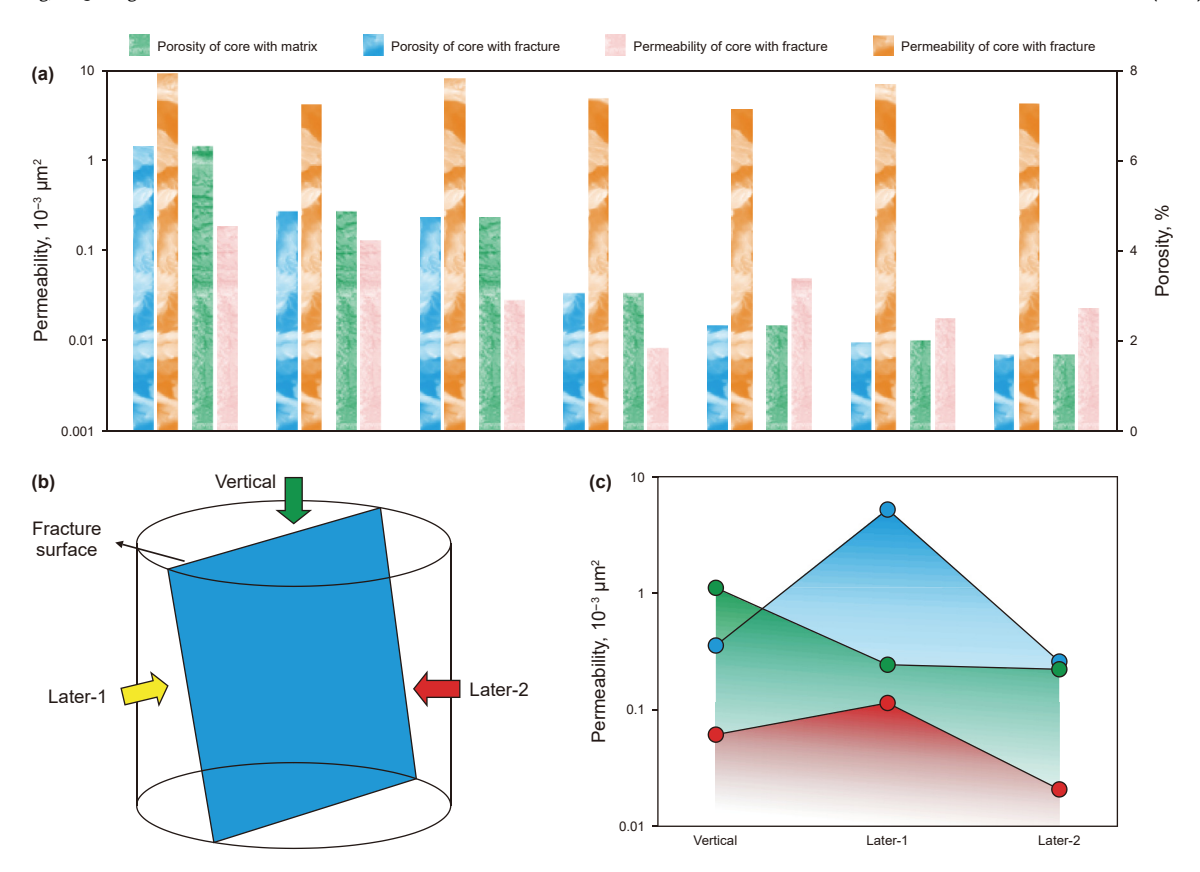


Fig. 15. (a) The histogram of core-measured physical properties of fracture samples and matrix samples. (b) The scatterplot of physical properties test of full diameter cores.

depth, vertical stress of the gypsum-salt strata is less than that of the sandstone/mudstone strata, which indicate the reduction of compaction.

Along with deep burial, high formation temperature makes gypsum-salt strong plasticity (Zhao and Wang, 2016), which can neutralize later tectonic compressive and form corresponding salt structure, like Dawanqi salt pillow (Fig. 1(d)). In addition, 3D prestack depth migration data also shows that almost all faults are suspended in gypsum rock and fail to pierce (Fig. 1(d) and 14).

Thermal conductivity of sandstone, mudstone and gypsum-salt are 1.7-3.1, 1.5-2.2, and $4.7 \, \text{W/(m \cdot K)}$, respectively (Wu et al., 2016). High thermal conductivity leads to rapid temperature conduction from the subsalt, resulting in formation temperature negative anomaly (Fig. 16(c)) and hysteresis of diagenesis in the subsalt. This is also the reason why the present burial depth exceeds 7000 m, while the corresponding formation temperature ranges from 140 to $150 \, ^{\circ}\text{C}$, and the diagenetic stage is only in the meso-diagenetic A (Fig. 9).

Gypsum can gradually dehydrate to form anhydrite, and accompanied by crystal water. The injection of crystal water effectively increases the pore fluid pressure. Owing to abnormal densification, displacement pressure and high breakthrough pressure (>60 MPa) of gypsum rock (Zhao et al., 2007; Li et al., 2021), overpressure is general in the subsalt. The thickness of gypsum rock ranges from 98 to 4887.5 m and the pressure coefficient is between 1.57 and 1.84, both show no clear relationship (Fig. 16(d)). In addition, as the strong alkaline fluid (including Ba²⁺, Ca²⁺, K⁺, Na⁺, SiO₄²⁻) permeates into the reservoir along faults-fractures-pores, anhydrite/dolomite cements/veins, and dissolution of siliceous are developed (Li et al., 2018). It can be seen that with the increase of the distance to the overlying gypsum rock, the content of secondary pores, anhydrite, and porosity decrease, and that of the siliceous increases (Fig. 17).

5.2.5. Overpressure

Overpressure can inhibit compaction and cementation, and can also form overpressure-related fractures (Zeng et al., 2016b; Stricker et al., 2016). However, its effects are not only related to its intensity, but also related to its formation time and evolution process (Grant et al., 2013; Nguyen et al., 2013). Previous studies have shown that overpressure developed since 5 Ma (Guo et al., 2016b).

Although porosity is the most intuitive manifestation of reservoir quality, porosity is always affected by various factors, including burial history, temperature, time, chemical reactions. The intergranular volume (IGV) is always used to reflect the strength of compaction, and then characterize the effects of overpressure on reservoir quality (Stricker et al., 2016; Xu et al., 2023). The overlying vertical stress is partially offset by the overpressure, and the rest is the effective stress exerted on the sandstones. The effective stress can indirectly reflect the overpressure strength. The IGV-effective stress trend of diagenetic facies A exhibits a negative correlation, while that of diagenetic facies B or diagenetic facies C is very random (Fig. 18). As shown in Fig. 9, owing to densification of diagenetic facies B and C before the formation of overpressure, there was not enough pore space for overpressure development in the late stage. Diagenetic facies B and C were free from overpressure effects. Conversely, With the on-set of the advanced overpressure, diagenetic facies A still retained certain pore space. With the increase of overpressure, the effective stress gradually decreased and partial pore space was preserved.

5.3. Differential evolution models of diagenetic facies

Sedimentation provides material basis for reservoir development. High-quality reservoirs are mainly distributed in the lower part of distributary channels and the upper part of mouth bar.

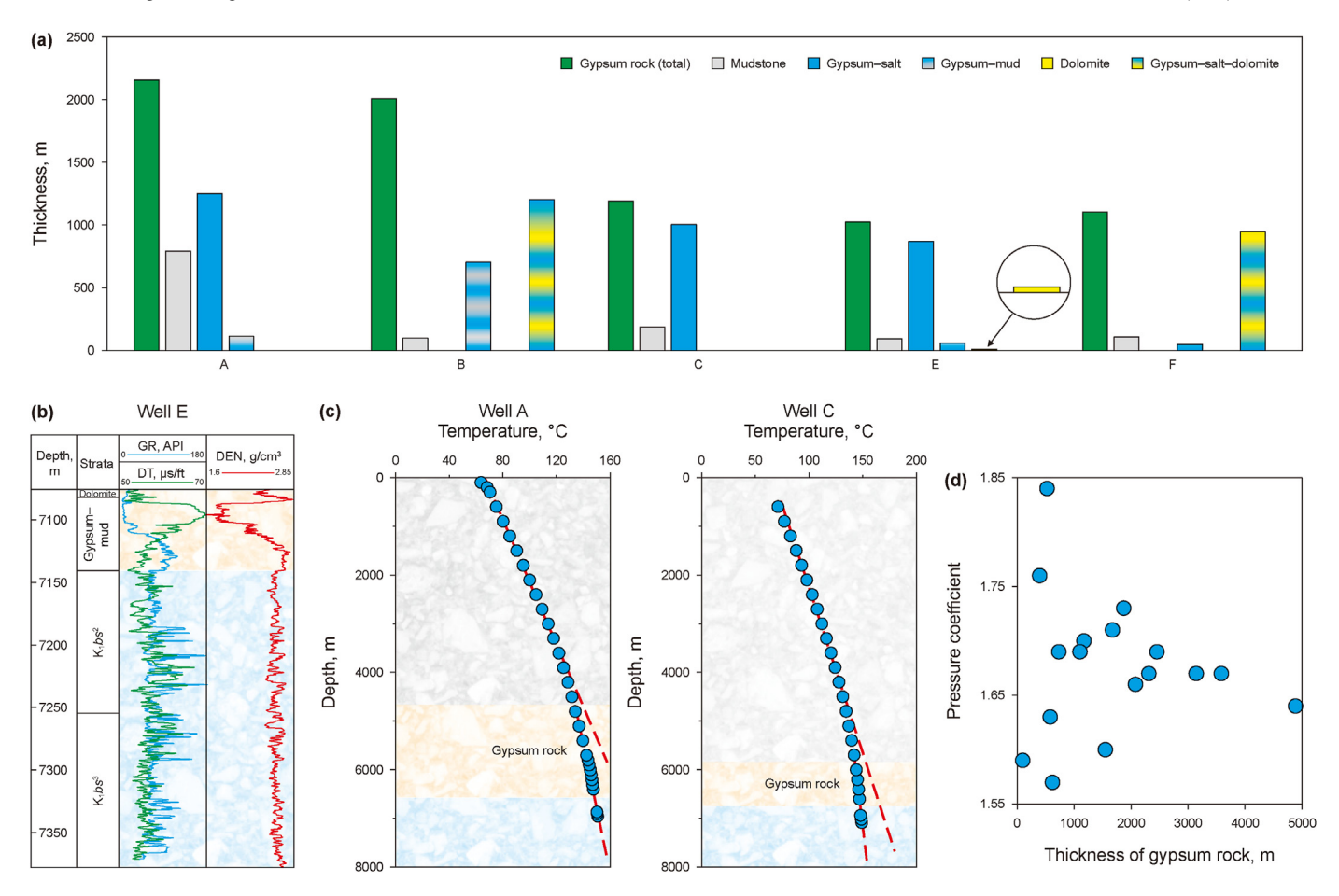


Fig. 16. (a) The thickness and composition of gypsum rock for different wells in the Dabei 3 gas reservoir. (b) Density logs of well E. (c) The scatter diagrams of burial depth and formation temperature of wells A and C. (d) The scatter diagram of the thickness of gypsum rock and pressure coefficient.

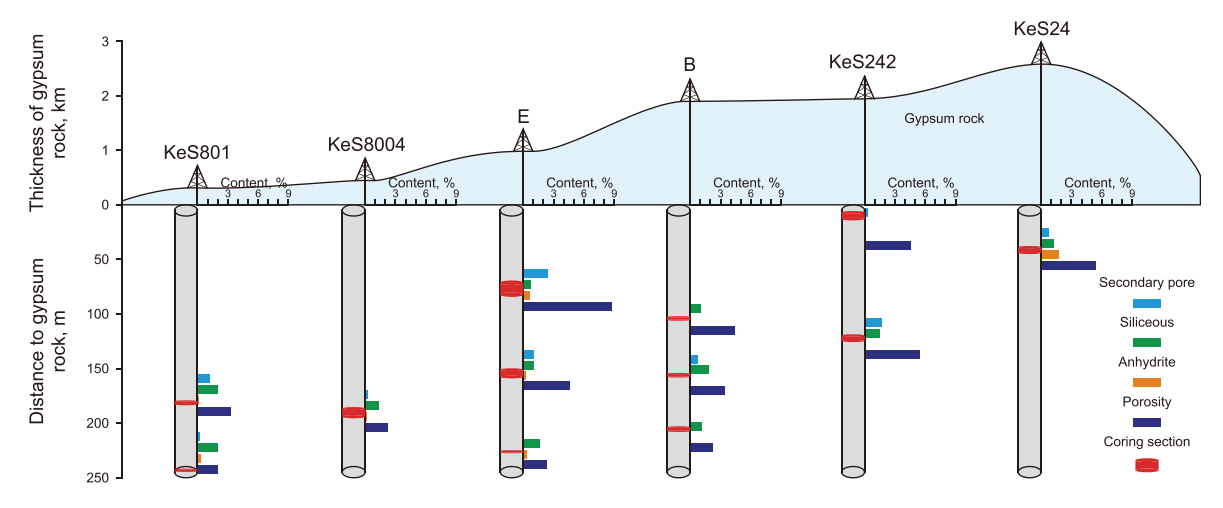


Fig. 17. The micro-petrological characteristics of cores corresponding to different thickness of gypsum rock and different distance from gypsum rock.

Diagenesis and tectonism are key factors for differential evolution of reservoir quality. Burial compaction, cementation and tectonic compression control reservoir densification. Natural fracture and dissolution improve reservoir quality. Combined with the diagenetic evolution sequence, the differential evolution model of ultradeep tight sandstone reservoir is established (Fig. 19).

Syndiagenesis-Eodiagenesis A: The reservoir was in slow shallow burial and was generally subjected to mechanical compaction (Fig. 9). Grains gradually came into close contact, and primary porosity was generally decreased. The strong deformation of matrix and mud gravel resulted in rapid decline of local porosity. During the deposition period of the Bashijiqik Formation, the

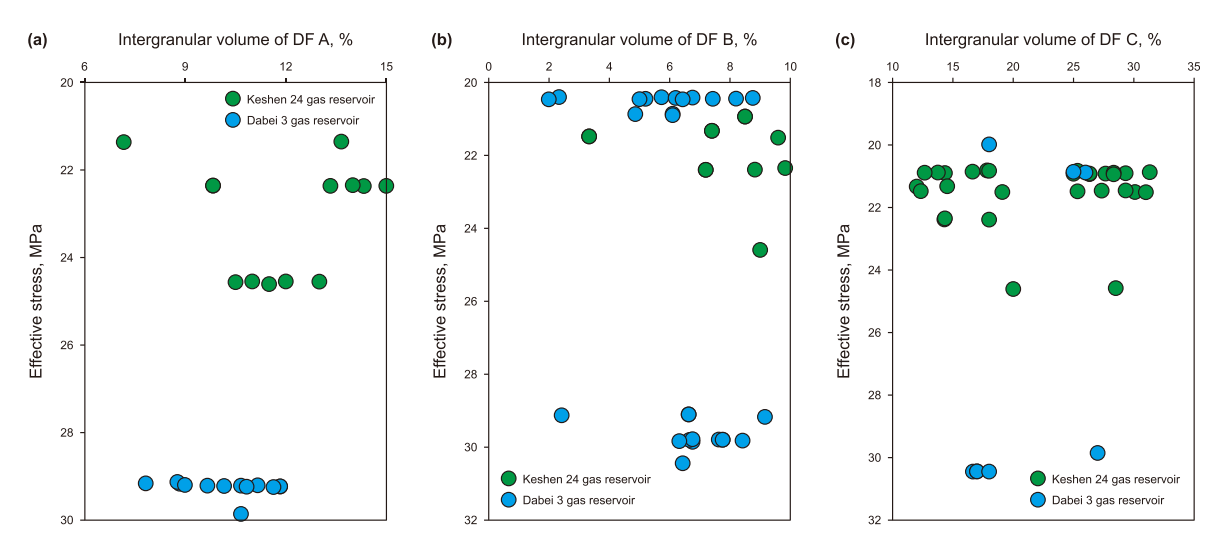


Fig. 18. The scatter diagrams of the intergranular volume and the effective stress for diagenetic facies A, B and C.

climate was hot and arid, and the sedimentary water was in saline state. Highly saline water led to the formation of hematite coating (Li et al., 2018).

Epidiagenesis: Controlled by the eluviation of atmospheric fresh water, partial feldspar and rock fragment were dissolved, resulting in secondary pores. The favorable physical property resulted in more secondary pores in diagenetic facies A. The concentration of Na⁺, K⁺, Ca²⁺, Mg²⁺, SiO₄²⁺ in formation water was increased by dissolution, which provided material basis for subsequent diagenetic cementation. With the weakening of eluviation, formation water gradually changed from acidic to alkaline.

Eodiagenesis: The reservoir underwent slow shallow burial once again (Fig. 9). Grains were in closer contact with each other by compaction. Pores were furtherly reduced. Controlled by tectonic compression, a few fractures were formed. For diagenetic facies B, deformation of ductile grains, mud gravel and matrix accelerated the densification. With the further increase of burial depth, diagenetic environment was gradually blocked, and the exchange of fluid was gradually weakened. The formation water remained alkaline, forming I-quartz/feldspar overgrowth and carbonate cements. Local calcite tightly cemented pores and metasomatic grains, resulting in diagenetic facies C. Poikilitic calcite also enhances compaction resistance and brittleness of diagenetic facies C. diagenetic facies C were susceptible to develop fractures by later tectonic compression. In addition, high thermal conductivity of gypsum-salt led to an abnormal formation temperature, and then delayed the diagenetic evolution of subsalt. I/S was gradually transformed into illite, with a large number of ions (Ca²⁺, Mg²⁺, SiO_4^{2-} , Al^{3+}) produced.

Mesodiagenesis A: The reservoir was in rapid deep burial (Fig. 9). Burial compaction resulted in a further porosity loss. Strong deformation of mud gravel, matrix, and ductile grains were squeezed into pores, forming pseudo-matrix. High formation temperature made gypsum dehydrate to form anhydrite, accompanied with large amounts of ions (Ca²⁺, K⁺, Na⁺, Al³, SiO₄²⁻). With the highly alkaline fluids injected into subsalt along unconformities and fractures, dolomite/anhydrite cements/veins and dissolution of siliceous gradually developed. Owing to close densification for diagenetic facies B, only a few cements developed locally. Diagenetic facies A had certain pore space for more cements. High temperature and high pressure accelerated the transformation of the I/S into illite. Strong tectonic compression led to the formation of numerous fractures in the late Himalaya period. Microfractures

mostly developed in diagenetic facies A, and tectonic fractures tended to develop in diagenetic facies B and C. Since 5–2 Ma, two successive phases of hydrocarbon charging occurred (Gao et al., 2016), and carried large amounts of CO₂. Massive CO₂ was injected, and the precipitation of illite consumed K⁺, resulting in a weak acid diagenetic environment. The selective corrosion of CO₂ resulted in dissolution of feldspar, and less dissolution of calcite (Li et al., 2018).

6. Conclusions

This study clarified the relationship between sedimentation, diagenesis, tectonism and reservoir quality to reveal the characteristic and controlling factors of high-quality reservoirs in the Bashijiqike Formation of the Dabei 3 gas reservoir. Differential diagenetic facies were used to understand differential diagenesis and differential evolution of reservoir quality of ultra-deep sandstone reservoirs. The conclusions were as follows:

Based on the texture and composition of detrital grains, authigenic minerals, diagenetic types and intensity, pore structure, coremeasured physical properties, gas saturation, sandstones are divided into three diagenetic facies: diagenetic facies A, diagenetic facies B, and diagenetic facies C.

Diagenetic facies B are mainly very fine to fine-grained sandstone, followed by mud-gravel-rich medium-grained sandstone. Due to the strong deformation of numerous ductile grains, Diagenetic facies B exhibits tight compaction. Diagenetic facies C is cemented by poikilitic carbonate cements, and exhibits tight cementation. Diagenetic facies B and C show extremely poor porosity, and can only be the barriers for hydrocarbon charging. Diagenetic facies A is mainly medium-fine to medium-grained sandstone. It has the good physical properties and excellent pore structure and gas bearing conditions, and is the high-quality reservoir for ultra-deep tight sandstone.

The gas reservoir exhibits gentle faulted anticline. The tectonic compression is lower than that of gas reservoirs close the south Tianshan orogenic belt. Porosity loss by tectonic compression is relatively smaller. Natural fractures can improve the permeability by multiple orders of magnitude. Gypsum rock can weaken the compaction, delay the cementation, and promote the overpressure. As the strong alkaline fluid permeates into the reservoir, anhydrite/dolomite cements/veins, and dissolution of siliceous are developed. Overpressure decrease the effective stress and preserve the

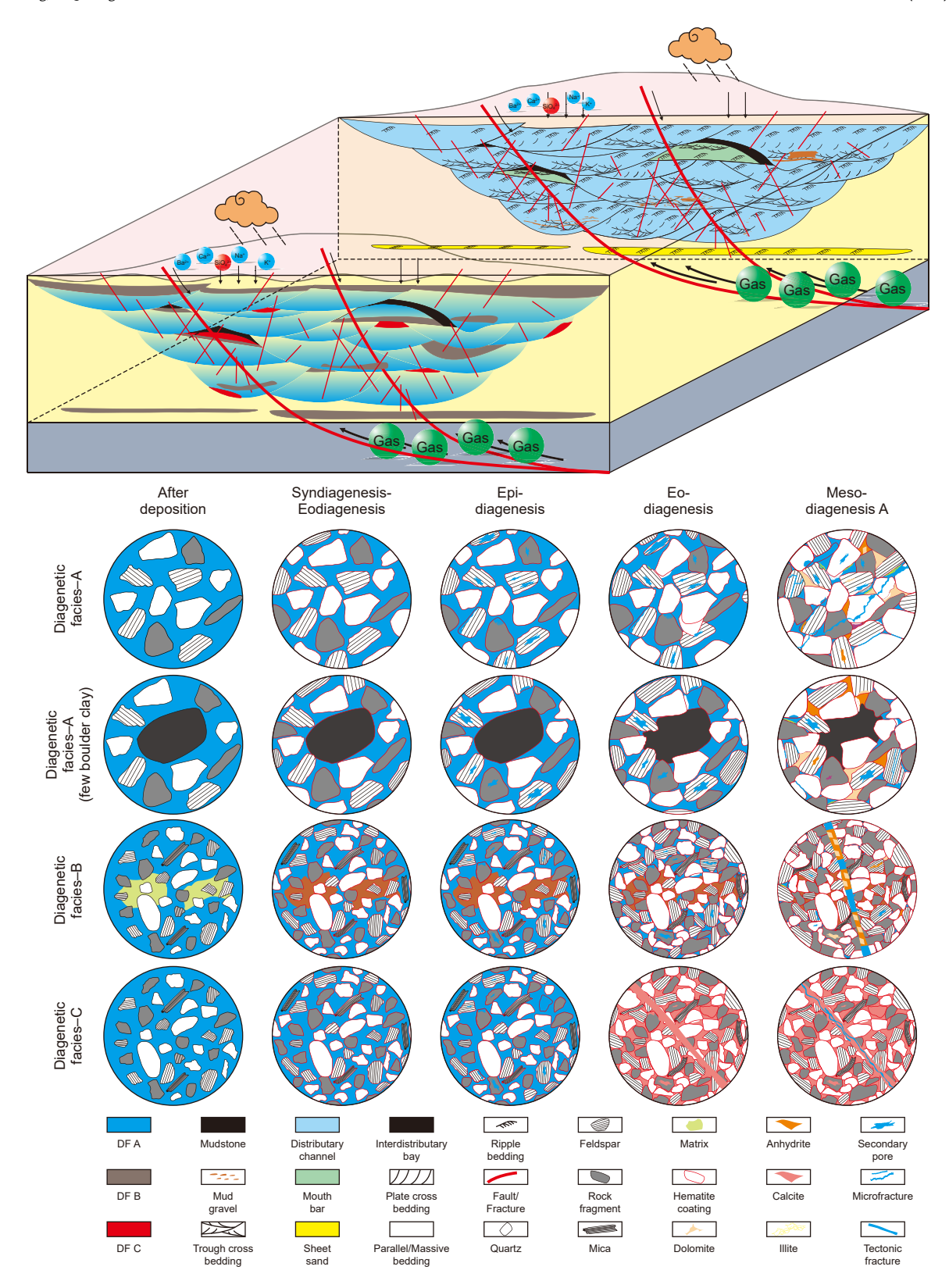


Fig. 19. Differential reservoir quality evolution model of different diagenetic facies.

porosity of Diagenetic facies A; Diagenetic facies B and C were tight early to be free from overpressure. Sedimentation provides the material basis for the high-quality reservoir. Diagenetic facies B is mainly distributed in sheet sand, partly in the upper part of distributary channel and the lower part of mouth bar. Diagenetic facies C is distributed randomly, and the overall thickness is thin and transverse discontinuous. Diagenetic facies A is mainly distributed in the middle and lower part of distributary channels

and the middle and upper part of mouth bar. This spatial combination model provides theoretical guidance for efficient exploration of ultra-deep tight sandstone effective reservoirs.

CRediT authorship contribution statement

Xiao-Tong Xu: Writing — review & editing, Writing — original draft, Visualization, Methodology, Formal analysis, Conceptualization. **Lian-Bo Zeng:** Writing — review & editing, Supervision, Methodology, Funding acquisition, Conceptualization. **Shao-Qun Dong:** Methodology, Formal analysis, Data curation. **Hai-Ming Li:** Supervision, Project administration, Methodology, Funding acquisition. **Jian-Zhong Liu:** Supervision, Project administration, Funding acquisition. **Chun-Qiu Ji:** Visualization, Software, Resources.

Data availability

Data will be made available on request.

Declaration of competing interest

The authors declare that they have no known competing financial interests or personal relationships that could have appeared to influence the work reported in this paper.

Acknowledgements

This article is supported by the National Natural Science Foundation of China, China (No. U21B2062). The author highly appreciates the data and support from the Exploration and Development Research Institute of PetroChina Tarim Oilfield Company, China. Thank the editor and several anonymous reviewers for their constructive comments, which have significantly contributed to the improvement of this article.

References

- Aase, N.E., Bjørkum, P.A., Nadeau, P.H., 1996. The effect of grain-coating microquartz on preservation of reservoir porosity. AAPG Bull. 80 (10), 1654–1673. https://doi.org/10.1306/64EDA0F0-1724-11D7-8645000102C1865D.
- Beard, D.C., Weyl, P.K., 1973. Influence of texture on porosity and permeability of unconsolidated sand. AAPG Bull. 57 (2), 349–369. https://doi.org/10.1306/ 819A4272-16C5-11D7-8645000102C1865D.
- Bjørlykke, K., 2014. Relationships between depositional environments, burial history and rock properties: some principal aspects of diagenetic process in sedimentary basins. Sediment. Geol. 301 (3), 1–14. https://doi.org/10.1016/isedgeo.2013.12.002.
- Bloch, S., Lander, R.H., Bonnell, L., 2002. Anomalously high porosity and permeability in deeply buried sandstone reservoirs: origin and predictability. AAPG Bull. 86 (2), 301–328. https://doi.org/10.1306/61EEDABC-173E-11D7-8645000102C1865D.
- Busch, B., Becker, I., Koehrer, B., Adelmann, D., Hilgers, C., 2019. Porosity evolution of two Upper Carboniferous tight-gas-fluvial sandstone reservoirs: impact of fractures and total cement volumes on reservoir quality. Mar. Petrol. Geol. 100, 376–390. https://doi.org/10.1016/j.marpetgeo.2018.10.051.
- Cao, B.F., Luo, X.R., Zhang, L.K., Sui, F.G., Lin, H.X., Lei, Y.H., 2017. Diagenetic heterogeneity of deep sandstone and its relationship to oil emplacement: a case study from the middle Jurassic Toutunhe formation in the Fukang Sag, central Junggar Basin (NW China). Geofluids 1–23. https://doi.org/10.1155/2017/4292079.
- Cao, B.F., Luo, X.R., Worden, R.H., Wang, X.Z., He, Y.H., Qiao, X.Y., Zhang, L.K., Lei, Y.H., Zhou, J.S., Deng, C., 2024a. Contrasting diagenetic evolution and hydrocarbon charge of tight gas sandstones in the lower Permian Shanxi Formation, southeastern Ordos Basin, China. J. Asian Earth Sci. 276, 106330. https://doi.org/10.1016/j.jseaes.2024.106330.
- Cao, B.F., Luo, X.R., Zhang, L.K., Lei, Y.H., Zhou, J.S., 2020. Petrofacies prediction and 3-D geological model in tight gas sandstone reservoirs by integration of well logs and geostatistical modeling. Mar. Petrol. Geol. 114, 104202. https://doi.org/ 10.1016/j.marpetgeo.2019.104202.
- Cao, B.F., Sun, W., Li, J., 2021. Reservoir petrofacies-A tool for characterization of reservoir quality and pore structures in a tight sandstone reservoir: a study from the sixth member of Upper Triassic Yanchang Formation, Ordos Basin,

- China. J. Petrol. Sci. Eng. 199, 108294. https://doi.org/10.1016/j.petrol.2020.108294.
- Cao, B.F., Luo, X.R., Wang, X., Zhang, L.Q., Shi, H., 2023. Calcite-cemented concretions in non-marine sandstones: an integrated study of outcrop sedimentology, petrography and clumped isotopes. Sedimentology 70 (4), 1039–1074. https:// doi.org/10.1111/sed.13071.
- Cao, Y.C., Yuan, G.H., Yang, H.J., Wang, Y.Z., Liu, K.Y., Zan, N.M., Xi, K.L., Wang, J., 2022. Current situation of oil and gas exploration and research progress of the origin of high-quality reservoirs in deep-ultra-deep clastic reservoirs of petroliferous basins. Acta Pet. Sin. 43 (1), 112—140. https://doi.org/10.7623/syxb202201010 (in Chinese).
- Cao, D.S., Zeng, L.B., Gomez-Rivas, E., Gong, L., Liu, G.P., Lu, G.Q., Bons, P.D., 2024b. Correction of linear fracture density and error analysis using underground borehole data. J. Struct. Geol. 184, 105152. https://doi.org/10.1016/ j.jsg.2024.105152.
- Dutton, S.P., Loucks, R.G., 2010. Diagenetic controls on evolution of porosity and permeability in Lower Tertiary Wilcox sandstones from shallow to ultradeep (200–6700 m) burial, Gulf of Mexico Basin. U. S. A. Mar. Petrol. Geol. 27, 69–81. https://doi.org/10.1016/j.marpetgeo.2009.12.010.
- Dutton, S.P., Loucks, R.G., Day-Stirrat, R.J., 2012. Impact of regional variation in detrital mineral composition on reservoir quality in deep to ultradeep lower Miocene sandstones, western Gulf of Mexico. Mar. Petrol. Geol. 35, 139–153. https://doi.org/10.1016/j.marpetgeo.2012.01.006.
- Ferraro, F., Agosta, F., Ukar, E., Grieco, D.S., Cavalcante, F., Belviso, C., Prosser, G., 2019. Structural diagenesis of carbonate fault rocks exhumed from shallow crustal depths: an example from the central-southern Apennines, Italy. J. Struct. Geol. 122, 58–80. https://doi.org/10.1016/j.jsg.2019.02.008.
- Gao, Z.Y., Feng, J.R., Cui, J.G., Wang, X.Q., Zhou, C.M., Shi, Y.X., 2017. Physical simulation and quantitative calculation of increased feldspar dissolution pores in deep reservoirs. Petrol Explor. Dev+. 44 (3), 387–398. https://doi.org/10.1016/S1876-3804(17)30045-9.
- Gao, Z.Y., Ma, J.Y., Cui, J.G., Feng, J.R., Zhou, C.M., Wu, H., 2018. Deep reservoir pore evolution model of a geological process from burial compaction to lateral extrusion. Acta Sedimentol. Sin. 36 (1), 176–187. https://doi.org/10.3969/j.issn.1000-0550.2018.019 (in Chinese).
- Gao, Z.Y., Zhou, C.M., Feng, J.R., Wu, H., Li, W., 2016. Mechanism and sedimentary environment of the muddy gravel concomitant with thick layer sandstone of Cretaceous in Kuqa depression. Acta Pet. Sin. 37 (8), 996–1010. https://doi.org/ 10.7623/syxb201608006 (in Chinese).
- Grant, N.T., Middleton, A.J., Archer, S., 2013. Porosity trends in the skagerrak formation, central graben, United Kingdom continental shelf: the role of compaction and pore pressure history. AAPG Bull. 98 (6), 1111–1143. https://doi.org/10.1306/10211313002.
- Grigsby, J.D., Langford, R.P., 1996. Effects of diagenesis on enhanced-resolution bulk density logs in Tertiary Gulf Coast sandstones: an example from the Lower Vicksburg Formation, McAllen Ranch field, south Texas. AAPG Bull. 80, 1801–1819. https://doi.org/10.1306/64eda172-1724-11d7-8645000102c1865d.
- Guo, S., Lyu, X.X., Zhang, Y., 2018. Relationship between tight sandstone reservoir formation and hydrocarbon charging: a case study of a Jurassic reservoir in the eastern Kuqa Depression, Tarim Basin, NW China. J. Nat. Sci. Eng. 52, 304—316. https://doi.org/10.1016/j.jngse.2018.01.031.
- Guo, X.W., Liu, K.Y., Jia, C.Z., Song, Y., Zhao, M.J., Zhuo, Q.G., Lu, X.S., 2016a. Constraining tectonic compression process by reservoir pressure evolution: over-pressure generation and evolution in the Kelasu Thrust Belt of Kuqa Foreland Basin, NW China. Mar. Petrol. Geol. 72, 30–44. https://doi.org/10.1016/j.marpetgeo.2016.01.015.
- Guo, X.W., Liu, K.Y., Jia, C.Z., Song, Y., Zhao, M.J., Zhuo, Q.G., Lu, X.S., 2016b. Fluid evolution in the Dabei gas field of the Kuqa Depression, Tarim Basin, NW China: Impactions for fault-related fluid flow. Mar. Petrol. Geol. 78, 1–16. https://doi.org/10.1016/j.marpetgeo.2016.08.024.
- Henares, S., Caracciolo, L., Viseras, C., Fernandez, J., Yeste, L.M., 2016. Diagenetic constraints on heterogeneous reservoir quality assessment: a Triassic outcrop analog of meandering fluvial reservoirs. AAPG Bull. 100 (9), 1377–1398. https:// doi.org/10.1007/s12182-009-0056-2.
- Hou, G.T., Sun, S., Zheng, C.F., Tang, Y.G., Zhou, L., Mo, T., 2019. Subsalt structural styles of Keshen section in Kelasu tectonic belt. Xinjiang Petroleum Geology 40 (1), 21–26. https://doi.org/10.7657/XJPG20190103 (in Chinese).
- Jia, C.Z., 2023. Key scientific and technological problems of petroleum exploration and development in deep and ultra-deep formation. Journal of China University of Petroleum (Edition of Natural Science) 47 (5), 1–12. https://doi.org/10.3969/ j.issn.1673-5005.2023.05.001 (in Chinese).
- Jia, C.Z., Zhang, R.H., Wei, G.Q., Wang, K., Yu, C.F., Zeng, Q.L., Si, X.Q., 2023. Reservoir-controlling effects of tectonic dynamics and ultra-deep reservoirs in Tianshan intracontinental thrust belt. Acta Pet. Sin. 44 (8), 1191–1205. https://doi.org/10.7623/syxb202308001 (in Chinese).
- Jiang, Z.L., Huang, S.Y., Du, H.L., Li, Y.J., Wang, B.Q., Cao, Y.T., Zhang, Y.F., 2015. The characteristics of the neotectonic movement and their effects on the formation of gas reservoirs in the marginal depressions of Tarim Basin, NW China. J. Nat. Sci. Eng. 22, 503–514. https://doi.org/10.1016/j.jngse.2014.12.028.
 Lai, J., Li, D., Ai, Y., Liu, H.K., Cai, D.Y., Chen, K.J., Xie, Y.Q., Wang, G.W., 2022.
- Lai, J., Li, D., Ai, Y., Liu, H.K., Cai, D.Y., Chen, K.J., Xie, Y.Q., Wang, G.W., 2022. Structural diagenesis in ultra-deep tight sandstones in the Kuqa Depression, Tarim Basin, China. Solid Earth 13, 975–1002. https://doi.org/10.5194/se-13-975-2022.
- Lai, J., Wang, G.W., Wang, S., Cao, J.T., Li, M., Pang, X.J., Zhou, Z.L., Fan, X.Q., Dai, Q.Q., Yang, L., He, Z.B., Qin, Z.Q., 2018. Review of diagenetic facies in tight sandstones:

- diagenesis, diagenetic minerals, and prediction via well logs. Earth Sci. Rev. 185, 234—258. https://doi.org/10.1016/j.earscirev.2018.06.009.
- Lai, J., Li, D., Bai, T.Y., Zhao, F., Ai, Y., Liu, H.K., Cai, D.Y., Wang, G.W., Chen, K.J., Xie, Y.Q., 2023. Reservoir quality evaluation and predication in ultra-deep tight sandstones in the Kuqa depression. J. Struct. Geol. 170, 104850. https://doi.org/ 10.1016/j.jsg.2023.104850.
- Lander, R.H., Bonnell, L.M., Larese, R.E., 2008. Toward more accurate quartz cement models: the importance of euhedral versus noneuhedral growth rates. AAPG Bull. 92 (11), 1537–1563. https://doi.org/10.1306/07160808037.
- Laubach, S.E., Eichhubl, P., Hilgers, C., Lander, R.H., 2010. Structural diagenesis. I. Struct. Geol. 32, 1866–1872. https://doi.org/10.1016/j.isg.2010.10.001.
- Li, J.H., Zhang, Y., Wang, H.H., Wang, D.J., 2020. Three-dimensional discrete element numerical simulation of Paleogene salt structures in the western Kuqa foreland thrust belt. Petrol. Explor. Dev+. 47 (1), 68–79. https://doi.org/10.1016/S1876-3804(20)60006-4.
- Li, L., Tang, H.M., Wang, X., Liao, J.J., Qi, B.L., Zhao, F., Zhang, L.H., Feng, W., Tang, H.X., Shi, L., 2018. Evolution of diagenetic fluid of ultra-deep cretaceous Bashijiqike Formation in Kuqa depression. J. Cent. South Univ. 25, 2472—2495. https://doi.org/10.1007/s11771-018-3930-5
- Li, W., Chen, Z.X., Huang, P.H., Yu, Z.C., Min, L., Lu, X.S., 2021. Formation of overpressure system and its relationship with the distribution of large gas fields in typical foreland basins in central and western China. Petrol. Explor. Dev+. 48 (3), 625–640. https://doi.org/10.1016/S1876-3804(21)60050-2.
- Li, Y., Guo, S., Wang, X., Hou, Y.F., Neng, Y., Wang, Z.X., Zhou, L., Yang, W.J., Tan, C., 2017. Stratification model of an ultra-deep tight sandstone fracture reservoir under tectonic stress: a case study of a Cretaceous reservoir in the Kuqa foreland thrust belt of the Tarim Basin. J. Nat. Sci. Eng. 45, 53–64. https://doi.org/ 10.1016/j.jngse.2017.05.010.
- Liu, Z.D., 2021. Research of Formation Mechanism of Deep-Ultra-Deep Sandstone Carrier and the Hydrocarbon Migration and Accumulation: an Example from the Kuqa Depression, Tarim Basin. Northeast Petroleum University, p. 199 (in Chinese).
- Lundegard, P.D., 1992. Sandstone porosity loss: a "Big Picture" view of the importance of compaction. J. Sediment. Res. 62 (2), 250–260. https://doi.org/10.1306/d42678d4-2b26-11d7-8648000102c1865d.
- Luo, X.R., Yang, H.J., Wang, Z.L., Zhang, L.Q., Zhang, L.K., Lei, Y.H., Zhou, L., Zhang, B.S., Yan, Y.M., Cao, B.F., Liu, Z.D., 2023a. Heterogeneity characteristics of clastic reservoirs and hydrocarbon accumulation mode in deep-ultradeep basins. Acta Geol. Sin. 97 (9), 2802–2819. https://doi.org/10.19762/j.cnki.dizhixuebao.2023207 (in Chinese).
- Luo, X.R., Zhang, L.K., Lei, Y.H., Hu, C.Z., Shi, H., Cao, B.F., 2016. Structural heterogeneity of reservoirs and its implication on hydrocarbon accumulation in deep zones. China Petroleum Exploration 21 (1), 28–36. https://doi.org/10.3969/j.issn.1672-7703.2016.01.003 (in Chinese).
- Luo, X.R., Zhang, L.K., Lei, Y.H., Yang, W., 2020. Petroleum migration and accumulation: modeling and applications. AAPG Bull. 104, 2247–2265. https://doi.org/10.1306/0422201618817104.
- Luo, X.R., Zhang, L.Q., Zhang, L.K., Lei, Y.H., Li, J., Yang, W., Cheng, M., Shi, H., Cao, B.F., 2023b. Heterogeneity in siliciclastic carrier beds: implications for hydrocarbon migration and accumulation. AAPG Bull. 107 (7), 1017–1036. https://doi.org/ 10.1306/10242221067.
- Nguyen, B.T.T., Jones, S.J., Goulty, N.R., Middleton, A.J., Grant, N., Ferguson, A., Bowen, L., 2013. The role of fluid pressure and diagenetic cements for porosity preservation in Triassic fluvial reservoir of the Central Graben, North Sea. AAPG Bull. 97 (8), 1273–1302. https://doi.org/10.1306/01151311163.
- Pettijohn, F.J., Potter, P.E., Siever, R., 1972. Sand and Sandstone. Springer-Verlag, Berlin.
- Pittman, E.D., Larese, R.E., 1991. Compaction of lithic sands: experimental results and applications. AAPG Bull. 75 (8), 1279—1299. https://doi.org/10.1306/ 0C9B292F-1710-11D7-8645000102C1865D.
- Pizzi, M., Whittaker, A.C., Mayall, M., Lonergan, L., 2023. Structural controls on the pathways and sedimentary architecture of submarine channels: new constraints from the Niger delta. Basin Res. 35 (1), 141–171. https://doi.org/10.1111/ bre 12707
- Pranter, M.J., Sommer, N.K., 2011. Static connectivity of fluvial sandstones in a lower coastal-plain setting: an example from the Upper Cretaceous lower Williams Fork Formation, Piceance basin, Colorado. AAPG Bull. 95 (6), 899–923. https:// doi.org/10.1306/12091010008.
- Qin, X., Chen, X.H., Shao, Z.G., Zhang, Y.P., Wang, Y.C., Li, B., 2022. Cenozoic multiphase intracontinental deformation of the Tianshan Range (NW China): constraints from detrital zircon provenance and syn-tectonic sedimentation of the Kuqa Depression. J. Asian Earth Sci. 232, 105183. https://doi.org/10.1016/ i.iseaes.2022.105183.
- Rushing, J.A., Newsham, K.E., Blasingame, T.A., 2008. Rock typing- keys to understanding productivity in tight gas sands: society of petroleum engineers unconventional reservoirs conference. Keystone, Colorado, February 10–12. SPE Paper 114164, 31pp.
- Shen, Y.Q., Lv, X.X., Guo, S., Zhan, J., 2017. Effective evaluation of gas migration in deep and ultra-deep tight sandstone reservoirs of Keshen structural belt, Kuqa depression. J. Nat. Sci. Eng. 46, 119–131. https://doi.org/10.1016/j.jngse.2017.06.033.
- Shou, J.F., Shen, Y., Zhang, H.L., Zhang, R.H., 2009. Characteristics of mesozoic-cenozoic tectonic diagenesis in the Kuqa area of the Tarim Basin, China. Pet. Sci. 6, 366–375. https://doi.org/10.1007/s12182-009-0056-2.

- Shou, J.F., Zhang, H.L., Shen, Y., Wang, X., Zhu, G.H., Si, C.S., 2006. Diagenetic mechanisms of sandstone reservoirs in China oil and gas-bearing basins. Acta Petrol. Sin. 22 (8), 2165–2170 (in Chinese).
- Song, Z.Z., Lv, M.Y., Zhao, L.B., Liu, C.Q., He, Y.Y., 2024. A novel bound water occurrence model for tight sandstone. Fuel 357, 130030. https://doi.org/10.1016/j.fuel.2023.130030.
- Stricker, S., Jones, S.J., Grant, N.T., 2016. Importance of vertical effective stress for reservoir quality in the Skagerrak Formation, central Graben, North Sea. Mar. Petrol. Geol. 78, 895–909. https://doi.org/10.1016/j.marpetgeo.2016.03.001.
- Taylor, T.R., Giles, M.R., Hathon, L.A., Diggs, T.N., Braunsdorf, N.R., Birbiglia, G.V., Kittridge, M.G., Macaulay, C.I., Espejo, I.S., 2010. Sandstone diagenesis and reservoir quality prediction: models, myths, and reality. AAPG Bull. 94 (8), 1093–1132. https://doi.org/10.1306/04211009123.
- Trask, P.D., 1930. Mechanical analyses of sediments by centrifuge. Econ. Geol. 25 (6), 581–599. https://doi.org/10.2113/gsecongeo.25.6.581.
- Vandeginste, V., Swennen, R., Allaeys, M., Ellam, R.M., Osadetz, K., Roure, F., 2012. Challenges of structural diagenesis in foreland fold-and-thrust belts: a case study on paleofluid flow in the Canadian Rocky Mountains West of Calgary. Mar. Petrol. Geol. 35, 235–251. https://doi.org/10.1016/j.marpetgeo.2012.02.014.
- Wang, B., Qiu, N.S., Littke, R., Amberg, S., Liu, Z.D., 2023. Petroleum system modelling in a compressional tectonic setting: the eastern Kuqa Depression, Tarim Basin, Northwestern China, J. Asian Earth Sci. 249, 105612. https://doi.org/10.1016/j.jseaes.2023.105612.
- Wang, K., Zhang, R.H., Zeng, Q.L., Wang, J.P., Xia, J.F., Mo, T., 2022. Characteristics and formation mechanism of Lower Cretaceous deep and ultra-deep reservoir in Bozi-Dabei area, Kuqa depression. J. China Inst. Min. Technol. 51 (2), 257–274. https://doi.org/10.13247/j.cnki.jcumt.001337.
- Weber, K.J., 1986. How heterogeneity affects oil recovery. In: Lake, L.W., Carroll, H, B (Eds.), Reservoir Characterization. Academic Press, Orlando, pp. 487–544. https://doi.org/10.1016/B978-0-12-434065-7.50021-6
- Wei, G.Q., Wang, J.P., Zeng, L.B., Tang, Y.L., Wang, K., Liu, T.T., Yang, Y., 2020. Structural reworking effects and new exploration discoveries of subsalt ultra-deep reservoirs in the Kelasu tectonic zone. Nat. Gas. Ind. 40 (1), 20–30 (in Chinese).
- Wei, G.Q., Wang, K., Zhang, R.H., Wang, B., Yu, C.F., 2022. Structural diagenesis and high-quality reservoir prediction of tight sandstones: a case study of the Jurassic Ahe Formation of the Dibei gas reservoir, Kuqa depression, Tarim basin, NW China. J. Asian Earth Sci. 239, 105399. https://doi.org/10.1016/ i.jseaes.2022.105399.
- William, R.D., Christopher, A.S., 1979. Plate tectonics and sandstone compositions. AAPG Bull. 63 (12), 2164–2182. https://doi.org/10.1306/2F9188FB-16CE-11D7-8645000102C1865D.
- Worden, R.H., Griffiths, J., Wooldridge, L.J., Utley, J.E.P., Lawan, A.Y., Muhammed, D.D., Simon, N., Armitage, P.J., 2020. Chlorite in sandstones. Earth Sci. Rev. 204, 103105. https://doi.org/10.1016/j.earscirev.2020.103105.
- Wu, H., Zhao, M.J., Zhuo, Q.G., Lu, X.S., Gui, L.L., Li, W.Q., Xu, Z.X., 2016. Quantitative analysis of the effect of salt on geothermal temperature and source rock evolution: a case study of Kuqa foreland basin, western China. Petrol. Explor. Dev+. 43 (4), 602–610. https://doi.org/10.1016/S1876-3804(16)30070-2.
- Xu, X.T., Zhang, L.K., Y, M.Z., Zhang, L.Q., Xiu, Z.L., Zeng, Z.P., Cao, B.F., Li, C., Lei, Y.H., Cheng, M., Hu, C.Z., 2021. Different diagenesis of deep sandstone reservoir and its relationship with reservoir property: case study of Jurassic in Zhengshacun area, central Junggar Basin. Nature Gas Geoscience 32 (7), 1022–1036. https://doi.org/10.11764/j.issn.1672-1926.2021.02.001 (in Chinese).
- Xu, X.T., Zhang, L.K., Zeng, L.B., Li, C., Zhang, L.Q., Zeng, Z.P., Ren, X.C., 2023. Effects of overpressure on deep sandstone reservoir quality: a case study of the Medium and Lower Jurassic formation in the Shawan Sag, central Junggar Basin, western China. Geoenergy Sci Eng 230, 212203. https://doi.org/10.1016/j.geoen.2023.212203.
- Yan, Y.M., Zhang, L.Q., Luo, X.R., Liu, K.Y., Jia, T., Lu, Y.J., 2023. Influence of the grain shape and packing texture on the primary porosity of sandstone: insights from a numerical simulation. Sedimentology 70 (6), 1856–1885. https://doi.org/ 10.1111/sed.13098.
- Yang, H.J., Shi, W.Z., Du, H., Shi, L.L., Wang, X., Dong, G.N., Mo, T., Zuo, T.N., Xu, L.T., Jiang, X.J., 2024. Hydrocarbon charging periods and maturities in Bozi-Dabei area of Kuqa depression and their indication to the structural trap sequence. Acta Pet. Sin. 45 (10), 1480—1491. https://doi.org/10.7623/syxb202410003 (in Chinese).
- Yang, X.J., 2011. Characteristics and Origin of Fractures in Tight Sandstone Reservoir with Low Permeability, Dabei Gas Field. China University of Petroleum (East China), p. 109.
- Yang, Z., Wu, S.H., Zhang, J.J., Zhang, K., Xu, Z.H., 2022. Diagenetic controls on the reservoir quality of tight reservoirs in digitate shallow-water lacustrine delta deposits: an example from the Triassic Yanchang Formation, southwestern Ordos Basin. China. Mar. Petrol. Geol. 144, 105839. https://doi.org/10.1016/ j.marpetgeo.2022.105839.
- Yuan, G.H., Cao, Y.C., Schulz, H.M., Hao, F., Gluyas, J., Liu, K.Y., Yang, T., Wang, Y.Z., Xi, K.L., Li, F.L., 2019. A review of feldspar alternation and its geological significant in sedimentary basins: from shallow aquifers to deep hydrocarbon reservoirs. Earth Sci. Rev. 191, 114–140. https://doi.org/10.1016/j.earscirev.2019.02.004.
- Zeng, L.B., 2004. Characteristics and petroleum geological significance of Himalayan orogeny in Kuqa foreland basin. Oil Gas Geol. 25 (2), 175–179 (in Chinese).
- Zeng, L.B., Gong, L., Guan, C., Zhang, B.J., Wang, Q.Q., Zeng, Q., Lyu, W.Y., 2022. Natural fractures and their contribution to tight gas conglomerate reservoirs: a

- case study in the northwestern Sichuan basin, China. J. Petrol. Sci. Eng. 210, 110028. https://doi.org/10.1016/j.petrol.2021.110028.
- Zeng, L.B., Lyu, W.Y., Li, J., Zhu, L.F., Weng, J.Q., Yue, F., Zu, K.W., 2016b. Natural fractures and their influence on shale gas enrichment in Sichuan basin, China. J. Nat. Gas Sci. Eng. 30, 1–9. https://doi.org/10.1016/j.jngse.2015.11.048.
- Zeng, L.B., Song, Y.C., Liu, G.P., Tan, X.L., Xu, X.T., Yao, Y.T., Mao, Z., 2023. Natural fractures in ultra-deep reservoirs of China: a review. J. Struct. Geol. 175, 104954. https://doi.org/10.1016/j.jsg.2023.104954.
- Zeng, L.B., Wang, H.J., Gong, L., Liu, B.M., 2010. Impacts of the tectonic stress field on natural gas migration and accumulation: a case study of the Kuqa Depression in the Tarim Basin. China. Mar. Petrol. Geol. 27 (7), 1616–1627. https://doi.org/ 10.1016/j.marpetgeo.2010.04.010.
- Zeng, L.B., Xu, X., Ma, S.J., Bao, H.Y., Tian, H., Mao, Z., Ostadhassan, M., Dong, S.Q., Lyu, W.Y., 2024. Contribution of lamellation fractures to porosity and permeability of shales: a case study of the Jiaoshiba area in the Sichuan Basin, China. Geoenergy Sci Eng 232, 212439. https://doi.org/10.1016/j.geoen.2023.212439.
- Zeng, L.B., Zhu, R.K., Gao, Z.Y., Gong, L., Liu, G.P., 2016a. Structural diagenesis and its petroleum geological significance. Petroleum Science Bulletin 1 (2), 191–197. https://doi.org/10.3969/j.issn.2096-1693.2016.02.015 (in Chinese).
- Zhang, L.K., Luo, X.R., Ye, M.Z., Zhang, B.S., Wei, H.X., Cao, B.F., Xu, X.T., Liu, Z.D., Lei, Y.H., Li, C., 2021a. Small-scale diagenetic heterogeneity effects on reservoir quality of deep sandstones: a case study from the Lower Jurassic Ahe formation, eastern Kuga depression. Geofluids, 6626652.

- Zhang, J.J., Wu, S.H., Hu, G.Y., Yue, D.L., Xu, Z.H., Chen, C., Zhang, K., Wang, J.J., Wen, S.Y., 2021c. Role of shale deformation in the structural development of a deepwater gravitational system in the Niger delta. Tectonics 40 (5), e2020TC006491. https://doi.org/10.1029/2020TC006491.
- Zhang, R.H., Wang, K., Zeng, Q.L., Yu, C.F., Wang, J.P., 2021b. Effectiveness and petroleum geological significance of tectonic fractures in the ultra-deep zone of the Kuqa foreland thrust belt: a case study of the Cretaceous Bashijiqike Formation in the Keshen gas field. Pet. Sci. 18(9), 728–741. https://doi.org/10.1007/s12182-021-00567-w.
- Zhang, Y., 2019. Tectonic-fluid Model of Deep Reservoir of Cretaceous in the Dabei Block, Kuqa Depression. China University of Petroleum, Beijing, p. 88 (in Chinese).
- Zhao, B., Wang, X., 2016. Evidence of early passive diapirism and tectonic evolution of salt structures in the western Kuqa depression (Quele area), southern Tianshan (NW China). J. Asian Earth Sci. 125, 138—151. https://doi.org/10.1016/j.jseaes.2016.05.021.
- Zhao, Z.Y., Zhou, Y.Q., Ma, X.M., Ji, G.S., 2007. The impact of saline deposit upon the hydrocarbon accumulation in petroliferous basin. Oil Gas Geol. 28 (2), 299–308 (in Chinese)
- Zou, C.N., Tao, S.Z., Zhou, H., Zhang, X.X., He, D.B., Zhou, C.M., Wang, L., Wang, X.S., Li, F.H., Zhu, R.K., Luo, P., Yuan, X.J., Xu, C.C., Yang, H., 2008. Genesis, classification and evolution method of diagenetic facies. Petrol. Explor. Dev+. 35 (5), 526–540. https://doi.org/10.1016/S1876-3804(09)60086-0.